

INFORMATION TO USERS

This manuscript has been reproduced from the microfilm master. UMI films the text directly from the original or copy submitted. Thus, some thesis and dissertation copies are in typewriter face, while others may be from any type of computer printer.

The quality of this reproduction is dependent upon the quality of the copy submitted. Broken or indistinct print, colored or poor quality illustrations and photographs, print bleedthrough, substandard margins, and improper alignment can adversely affect reproduction.

In the unlikely event that the author did not send UMI a complete manuscript and there are missing pages, these will be noted. Also, if unauthorized copyright material had to be removed, a note will indicate the deletion.

Oversize materials (e.g., maps, drawings, charts) are reproduced by sectioning the original, beginning at the upper left-hand corner and continuing from left to right in equal sections with small overlaps. Each original is also photographed in one exposure and is included in reduced form at the back of the book.

Photographs included in the original manuscript have been reproduced xerographically in this copy. Higher quality 6" x 9" black and white photographic prints are available for any photographs or illustrations appearing in this copy for an additional charge. Contact UMI directly to order.

U·M·I

University Microfilms International
A Bell & Howell Information Company
300 North Zeeb Road, Ann Arbor, MI 48106-1346 USA
313/761-4700 800/521-0600



Order Number 1349459

The polarized light scattering matrix elements for rough surface

Hsu, Jiunn-Yann, M.S.

The University of Arizona, 1992

U·M·I
300 N. Zeeb Rd.
Ann Arbor, MI 48106

**THE POLARIZED LIGHT SCATTERING MATRIX
ELEMENTS
FOR ROUGH SURFACE**

by

Jiunn-Yann Hsu

A Thesis Submitted to the Faculty of the
DEPARTMENT OF PHYSICS
In Partial Fulfilment of the Requirements
For the Degree of
MASTER OF SCIENCE
In the Graduate College
THE UNIVERSITY OF ARIZONA

1 9 9 2

STATEMENT BY AUTHOR

This thesis has been submitted in partial fulfillment of requirements for an advanced degree at The University of Arizona and is deposited in the University Library to be made available to borrowers under rules of the library.

Brief quotations from this thesis are allowable without special permission, provided that accurate acknowledgment of the source is made. Requests for permission for extended quotation from or reproduction of thesis manuscript in whole or in part may be granted by the head of the major department or the Dean of the Graduate College when in his or her judgment the proposed use of the material is in the interests of scholarship. In all other instances, however, permission must be obtained from the author.

SIGNED: *Jim-Yann Asan*

APPROVAL BY THESIS DIRECTOR

This thesis has been approved on the date shown below:

William S. Bickel
William S. Bickel
Professor of Physics

July 28 1992
Date

ACKNOWLEDGMENTS

With earnest sincerity, I would, first of all, like to thank Prof. William S. Bickel for his advice, encouragement, and favorable help throughout all stages of my graduate work. Without his endless support and guidance this thesis would not have been possible.

I would like to thank Shu-Chung Chiao for his helpful assistance in this work.

Special thanks also go to Mr. Gary Chandler for his expertise regarding the SEM used in this work.

I would like to thank the U.S. Army Research Office (Grant DAAL03-86-D-0001) and Air Force Office of Scientific Research (Grant 90-NE-020) for their support of this research.

Thanks also are due to Tsung-Hsun Tsai for his helping me use the \LaTeX program when preparing this manuscript.

Finally, I would especially like to thank my parents, all my family members, and Hwei-Chuan Yang for their support, understanding, and encouragement over these years.

TABLE OF CONTENTS

LIST OF FIGURES	6
LIST OF TABLES	9
ABSTRACT	10
1. INTRODUCTION	11
2. MATHEMATICAL DESCRIPTION OF POLARIZATION	14
2.1. Polarization	14
2.2. Stokes Vectors	16
2.3. Mueller Matrices	21
3. REFLECTION AND REFRACTION OF ELECTROMAGNETIC WAVES	27
3.1. Reflection and Refraction at Surface of a Non-absorbing Medium	27
3.2. Reflection at the Surface of an Absorbing Medium	33
3.3. Diffuse Reflection	34
3.4. The Relation Between Fresnel Coefficients and Scattering Matrix Elements	36
4. NEPHELOMETER TECHNIQUE	37
4.1. Polarization Modulation Techniques	40
4.1.1. The Modulator	40
4.2. Lock-in Detection and Electronic System	47
4.2.1. The Constant Current Servo	47
4.2.2. Lock-in Amplifier	48
4.3. The Experimental Matrix $S_{ij}^*(\theta)$	50
4.4. Calibration	50
5. SAMPLE PREPARATION	55
6. THE MEASUREMENTS	63
7. RESULTS	78
7.1. Mueller Matrix Elements for Rough Surface	78
7.2. Change Index of Reflection for Rough Surface	81

7.2.1. 45° Incidence	81
7.2.2. 90° Incidence	82
7.3. Conclusion	83
7.3.1. Sandblasted Aluminum Rough Surface	83
7.3.2. Diffuse Surface	84
APPENDIX A. SCANNING ELECTRON MICROSCOPE TECHNIQUE	93
A.1. Introduction	93
A.2. Principle of the Scanning Electron Microscope	93
A.3. Operation Parameters of using ISI Super III-A SEM	96
REFERENCES	99

LIST OF FIGURES

3.1. Incident wave \vec{K} strikes plane interface between two different media, giving rise to a refracted wave \vec{K}' and a reflected \vec{K}''	28
3.2. Electric field perpendicular to the plane of incidence.	31
3.3. Electric field parallel to the plane of incidence.	32
4.1. Schematic diagram of nephelometer setup.	38
4.2. Orientations of the optical elements required to measure S_{ij}	51
4.3. Calibration orientations and lock-in frequencies to measure matrix elements.	52
5.1. Micrograph of the glass sand which was used to create the aluminum rough surface.	56
5.2. Micrograph of smooth surface sample # 0.	57
5.3. Micrograph of sample # 1 substrate roughened by sandblasting.	57
5.4. Micrograph of sample # 2 substrate roughened by sandblasting.	58
5.5. Micrograph of sample # 3 substrate roughened by sandblasting.	58
5.6. Micrograph of sample # 4 substrate roughened by sandblasting.	59
5.7. Micrograph of sample # 5 substrate roughened by sandblasting.	59
5.8. Micrograph of sample # 6 substrate roughened by sandblasting.	60
5.9. Micrograph of sample # 7 substrate roughened by sandblasting.	60
5.10. Micrograph of diffuse surface sample # 10.	61
5.11. Micrograph of aluminum coated diffuse surface sample # 11.	62
6.1. Experimental measurements of the sixteen light scattering Mueller matrix elements of a substrate # 4 (slightly roughened) illuminated at grazing incident angle $\alpha \approx 15^\circ$ ($\lambda = 441.6nm$).	65
6.2. Experimental measurements of the four light scattering Mueller matrix elements of a substrate # 0 illuminated at $\alpha = 15^\circ, 30^\circ, 45^\circ, 60^\circ$, and 75° ($\lambda = 441.6nm$).	66
6.3. Experimental measurements of the four light scattering Mueller matrix elements of a substrate # 1 illuminated at $\alpha = 15^\circ, 30^\circ, 45^\circ, 60^\circ$, and 75° ($\lambda = 441.6nm$).	67
6.4. Experimental measurements of the four light scattering Mueller matrix elements of a substrate # 2 illuminated at $\alpha = 15^\circ, 30^\circ, 45^\circ, 60^\circ$, and 75° ($\lambda = 441.6nm$).	68

6.5. Experimental measurements of the four light scattering Mueller matrix elements of a substrate # 3 illuminated at $\alpha = 15^\circ, 30^\circ, 45^\circ, 60^\circ$, and 75° ($\lambda = 441.6nm$).	69
6.6. Experimental measurements of the four light scattering Mueller matrix elements of a substrate # 4 illuminated at $\alpha = 15^\circ, 30^\circ, 45^\circ, 60^\circ$, and 75° ($\lambda = 441.6nm$).	70
6.7. Experimental measurements of the four light scattering Mueller matrix elements of a substrate # 5 illuminated at $\alpha = 15^\circ, 30^\circ, 45^\circ, 60^\circ$, and 75° ($\lambda = 441.6nm$).	71
6.8. Experimental measurements of the four light scattering Mueller matrix elements of a substrate # 6 illuminated at $\alpha = 15^\circ, 30^\circ, 45^\circ, 60^\circ$, and 75° ($\lambda = 441.6nm$).	72
6.9. Experimental measurements of the four light scattering Mueller matrix elements of a substrate # 7 illuminated at $\alpha = 15^\circ, 30^\circ, 45^\circ, 60^\circ$, and 75° ($\lambda = 441.6nm$).	73
6.10. Experimental measurements of the sixteen light scattering Mueller matrix elements of a diffuse surface # 10 (before aluminum coating) illuminated at $\alpha = 45^\circ$	74
6.11. Experimental measurements of the sixteen light scattering Mueller matrix elements of an aluminum coated diffuse surface # 11 illuminated at $\alpha = 45^\circ$	75
6.12. Experimental measurements of the sixteen light scattering Mueller matrix elements of a diffuse surface # 10 (before aluminum coating) illuminated at $\alpha = 90^\circ$	76
6.13. Experimental measurements of the sixteen light scattering Mueller matrix elements of an aluminum coated diffuse surface # 11 illuminated at $\alpha = 90^\circ$	77
7.1. The experimentally measured Mueller matrix elements for sand measured at three different positions on the surface (illuminated at grazing incidence).	89
7.2. The experimentally measured Mueller matrix elements for sandy soil measured at three different positions on the surface (illuminated at grazing incidence).	90
7.3. The experimentally measured Mueller matrix elements for clay soil measured at three different positions on the surface (illuminated at grazing incidence).	91
7.4. The experimentally measured Mueller matrix elements for loamy soil measured at three different positions on the surface (illuminated at grazing incidence).	92
A.1. Schematic drawing of the electron and x-ray optics of a combined SEM-EPMA.	95

A.2. Example of two different magnifications of a metal grid with symmetric geometry.	97
---	----

LIST OF TABLES

5.1. Measured rms surface roughness (σ) for samples.	56
7.1. The distinguishing ability of the four Mueller matrix elements for illumination angles and surface roughness	85
7.2. The distinguishing ability of the Mueller matrix elements for non-absorbing and absorbing diffuse surface.	86
7.3. Ingredient and size range of particles in four soils.	88

ABSTRACT

The light scattered from a scatterer depends on the geometrical properties such as size, shape, and their distributions as well as electromagnetic properties such as the complex index of reflection. The four major Mueller scattering matrix elements have been experimentally measured for an aluminum rough surface scattering laser light at $\lambda = 441.6nm$ for various incident angles. Measurements were also made for non-conducting diffuse surface and an aluminum coated diffuse surface. The sixteen Mueller matrix elements of these diffuse surfaces were measured in order to study the relative role of reflectance and roughness for scattering from a rough surface. Some representative matrix elements for the rough surfaces as well as for conducting and non-conducting rough surfaces are shown. S_{11} , and S_{34} are sensitive to illumination angles and surface variation. S_{33} are sensitive to illumination angles only. S_{34} are very sensitive to the change of refractive index from real to complex.

CHAPTER 1

INTRODUCTION

The scattering of the light is a natural phenomenon. We know the sky is blue because of the scattering of the solar rays by the air molecules. Otherwise the heavens would be black. This phenomenon was understood around 1500 by Leonardo da Vinci through his experiments with the scattering of sunlight by wood smoke observed against a dark background. In 1871, Lord Rayleigh was interested in the scattering of light by particles in the earth's atmosphere. He conceived a sphere as being the simplest model for such scatterers, and gave the quantitative explanation of the blue sky.

Bartholinus, a Danish scientist, discovered polarized light. He observed the effect of double refraction which occurred when the light passed through a calcite crystal. This crystal separated natural light into two perpendicularly polarized components and sent them in different directions which caused a double image. This description was very important for both Newton and Huygens in their investigations of the natural light. The complete explanation of polarization was made by Young. He suggested that the ether must have transverse vibrations. In the mean time, Malus passed partially reflected light through a calcite crystal and found that it was polarized. Malus took Newton's idea about how double reflection might be because the "particles of light" were asymmetric to

explain the double-reflection and partial-reflection phenomena. He considered the “light particles” to be randomly oriented before they passed through a double-refracting crystal. The particles would align and become ordered, after passing through the crystal. Brewster also measured the polarized intensities at various angles of incidence.

Now we know most of light around us is partially polarized. Scattering of the sun’s rays can produce the polarization. The reflecting surfaces in nature that are “horizontal” produce the reflecting light with polarization in the horizontal direction. Eye glasses that are coated with a film which transmits only the vertical polarized light will remove the most of the reflected light. These are called polarizing sunglasses. The calcite crystal can be used as a linear polarizer. When an electromagnetic wave is incident on a plane, it reflects according to the law of reflection. The reflected EM field depends on the wavelength, the angle of incidence and the electrical properties of this plane. Normally the law of reflection by a plane can be solved, and the electrical properties of material can be determined from the wavelength dependent reflection coefficient.

Dirt, scratches, and other defects can make a smooth surface rough. When the plane is not smooth, flat, and specular, the light incident on it is scattered. If the irregular surface is not too rough, the reflected light is composed of a specular component and a diffuse component which is scattered over a wide range of angles centered around the specular peak.

Vincent Iafelice and William Bickel (1987) studied the polarized light scattering matrix elements for select perfect and perturbed optical surfaces[1]. They studied two kinds of ideal surfaces. One was a perfect optical surface which reflects the propagation wave in

the specular direction as determined by the law of reflection. The other was a perfectly diffuse reflector which scatters light according to Lambert's cosine law. The intensity in any direction varies as the cosine of the angle between that direction and the normal to the surface. Usually, a real life rough surface scatters light with the scattered intensity falling anywhere between the two ideal cases. They also compared their experimental results with existing theories.

This thesis deals mainly with the scattering of light from rough surfaces and coated rough surfaces. Our data are represented in the context of the Mueller light scattering matrix elements.

CHAPTER 2

MATHEMATICAL DESCRIPTION OF POLARIZATION

2.1 Polarization

The electromagnetic wave \vec{E} and \vec{H} can be expressed as

$$\vec{E} = \vec{E}_0 \exp i(\vec{k} \cdot \vec{r} - \omega t)$$

$$\vec{H} = \vec{H}_0 \exp i(\vec{k} \cdot \vec{r} - \omega t)$$

If the amplitudes \vec{E}_0 and \vec{H}_0 are constant and real vectors, the electromagnetic wave is said to be linearly polarized. Therefore, the EM wave can be completely described by specifying its frequency, amplitude, direction, phase, and state of polarization. In daily life, the more common unpolarized light can be represented by light whose instantaneous polarization fluctuates rapidly in a random manner.

Consider the special case of two linearly polarized waves of same amplitude E_0 , polarized orthogonal to each other with phase difference between these two waves of $\frac{\pi}{2}$. Choose the electric vectors of the two waves to be in the x and y direction, respectively. Then the total electric field is the vector sum of the two component fields.

$$\vec{E} = E_0[\hat{x} \cos(kz - \omega t) + \hat{y} \sin(kz - \omega t)] \quad (2.1)$$

This type of wave can be treated as single wave in which the electric vector at a given point is constant in magnitude but rotates with the angular frequency ω . The wave is said to be circularly polarized. The device for creating circular polarized light is a quarter wave plate. The plate is made of a double refractive transparent crystal, which has the property that the index of refraction is different for the two different directions of polarization. The crystal is cut into a slab so that the axis of larger index n_1 (the slow axis) and the axis of smaller index n_2 (the fast axis) lie at right angles to one another in the plane of slab. If the slab thickness is d , then the optical paths are n_1d for light polarized in the direction of slow axis and n_2d for light polarized in the direction of the fast axis. To make a quarter-wave plate, d is chosen to make the difference of $n_1d - n_2d$ equal to one fourth of the wavelength incident on the plate.

$$d(n_1 - n_2) = \frac{\lambda_0}{4}$$

or

$$d = \frac{\lambda_0}{4(n_1 - n_2)}$$

The circular polarized light is thus produced by a phase shift of $\frac{\pi}{2}$ between two orthogonal components of linear polarized light.

If the amplitudes of the components $\hat{x}E_0 \cos(kz - \omega t)$ and $\hat{y}E'_0 \sin(kz - \omega t)$ in Equation 2.1 are not the same, i.e. $E_0 \neq E'_0$, at a given point in space, the resultant electric vector will both rotate and change in magnitude. The end of the rotating E vector describes an ellipse. The wave is called elliptically polarized. If we let \vec{E}_0 be a complex vector amplitude

$$\vec{E}_0 = \hat{x}E_0 + i\hat{y}E'_0,$$

then the electromagnetic wave

$$\vec{E} = \vec{E}_0 \exp i(kz - \omega t)$$

can be used to represent any type of polarization.

1. If \vec{E}_0 is real, the wave is linearly polarized.
2. If \vec{E}_0 is complex, the wave is elliptically polarized.
3. If the real part and imaginary part are equal, the wave is circularly polarized.

2.2 Stokes Vectors

A powerful representation of polarized light was developed by G. G. Stokes in 1852. He introduced four quantities which are functions of the observables of an electromagnetic wave. These four quantities are the components of the Stokes vector. They are very convenient to describe the different kinds of polarization, especially with regard to the light scattering calculation. The vectors describe the intensity and polarization states of the light. A beam of light may be polarized completely, partially, or it can be unpolarized. These four quantities are time-averaged intensity. The average of intensity is taken over a period long enough to get a practical measurement. They are denoted by a column vector as

$$\begin{pmatrix} I \\ Q \\ U \\ V \end{pmatrix}$$

The four quantities I , Q , U , and V are called total intensity, horizontal polarization, $+45^\circ$ polarization, right-circular polarization respectively. A parameter with a negative value represents the orthogonal state of polarization. For example, if V has the value -0.5 , the polarization is left-circular polarization instead of right-hand circular polarization.

The basic way to define the Stokes vector is to use four polarizing filters called F_1 , F_2 , F_3 , and F_4 . Each filter except F_1 transmits half of the incident unpolarized light. Each filter can be oriented so that its surface is perpendicular to the incident beam and rotated through angle ϕ about the beam axis. F_1 is isotropic, essentially a sheet of glass or clear aperture. It has the same effect on the incident beam in any orientation. The transmission axis of polarizer F_2 is horizontal. Polarizer F_3 is opaque to the light polarized at -45° , and transmits only $+45^\circ$ light. The last filter F_4 is a circular polarizer which is opaque to left-circular polarized light. It transmits only right-circular polarized light.

The operational definition of the Stokes parameter is given by the following relations[2]

$$I = I_0$$

$$Q = 2I_1 - I_0$$

$$U = 2I_2 - I_0$$

$$V = 2I_3 - I_0$$

where I_0 , I_1 , I_2 , and I_3 are the intensities of light which the F_1 , F_2 , F_3 , and F_4 polarizers transmit. These are individually measured by the detector. I is the incident irradiance while Q , U , and V specify the state of polarization. $Q > 0$ represents a horizontal polarization state; $Q < 0$ represents a vertical polarization state. When $Q = 0$, the

transmitted beam is independent of the orientation of horizontal and vertical axes. The state of the beam could be at $\pm 45^\circ$, right or left circular, or unpolarized. U represents the orientation of transmitted light in the state of $+45^\circ$ ($U > 0$), -45° ($U < 0$) or neither of $\pm 45^\circ$ ($U = 0$). V represents the transmitted light right-circular ($V > 0$), left-circular ($V < 0$) or neither ($V = 0$).

If we use the electric field to describe the polarization state of the incident light, the Stokes parameters can be defined as following

$$\begin{aligned}
 I &= E_x E_x^* + E_y E_y^* \\
 &= a_x^2 + a_y^2 \\
 Q &= E_x E_x^* - E_y E_y^* \\
 &= a_x^2 - a_y^2 \\
 U &= E_x E_y^* + E_y E_x^* \\
 &= 2a_x a_y \cos \delta \\
 V &= i(E_x E_y^* - E_y E_x^*) \\
 &= 2a_x a_y \sin \delta
 \end{aligned}$$

where

$$\begin{aligned}
 \vec{E} &= \vec{E}_0 \exp i(kz - \omega t) \\
 \vec{E}_0 &= \hat{x} E_x + \hat{y} E_y \\
 E_x &= a_x \exp(-i\delta_x) \\
 E_y &= a_y \exp(-i\delta_y)
 \end{aligned}$$

$$k = \frac{2\pi}{\lambda}$$

λ = wavelength of light

ω = angular frequency of the light

a_x, a_y = amplitudes of the electric field

δ_x, δ_y = The phase angles of the two complex amplitudes

δ = $\delta_x - \delta_y$, is the phase difference between two field components

When the filter F_1 is in the beam, the detector sees I_0 and I_0 is the same as I . From the definition, the irradiance I of the incident beam is

$$\begin{aligned} I &= |\vec{E}|^2 = |\vec{E}_0|^2 \\ &= (\hat{x}E_x + \hat{y}E_y) \cdot (\hat{x}E_x + \hat{y}E_y)^* \\ &= E_x E_x^* + E_y E_y^* \\ &= a_x^2 + a_y^2 \end{aligned}$$

With the filter F_2 is in, only the x component of the electric field is transmitted and the detector sees the irradiance $I_1 = E_x E_x^*$

$$\begin{aligned} Q &= 2I_1 - I_0 \\ &= 2E_x E_x^* - (E_x E_x^* + E_y E_y^*) \\ &= E_x E_x^* - E_y E_y^* \\ &= a_x^2 - a_y^2 \end{aligned}$$

When the filter F_3 is in, only the $+45^\circ$ of the electric field is transmitted and the detector sees the irradiance I_2 . As we know, any polarization form can be represented by

a linear combination of two vectors representing orthogonal polarization forms. Although the light vector is usually written as a linear combination of horizontal and vertical polarizations, it can be expressed as a linear combination of $+45^\circ$ and -45° components, right and left circular components, or any other two components that satisfy the conditions of orthogonality. In this case we need to transform the representation of the electric vector from x, y axes into the sum of $+45^\circ$ and -45° .

$$\begin{aligned}
I_2 &= \frac{1}{\sqrt{2}}(E_x + E_y) \frac{1}{\sqrt{2}}(E_x + E_y)^* \\
&= \frac{1}{2}(E_x E_x^* + E_y E_y^* + E_x E_y^* + E_y E_x^*) \\
U &= 2I_2 - I_0 \\
&= (E_x E_x^* + E_y E_y^* + E_x E_y^* + E_y E_x^*) - (E_x E_x^* + E_y E_y^*) \\
&= E_x E_y^* + E_y E_x^* \\
&= [a_x \exp(-i\delta_x) a_y \exp(i\delta_y) + a_y \exp(-i\delta_y) a_x \exp(i\delta_x)] \\
&= a_x a_y \{ \exp(-i(\delta_x - \delta_y)) + \exp(i(\delta_x - \delta_y)) \} \\
&= 2a_x a_y \cos \delta
\end{aligned}$$

When the filter F_4 , a right-circular polarizer, is in. The beam is converted to circularly polarized light. When the electric field rotates clockwise as we looking at the beam, this light is defined as right-circular polarization. Right-circular polarization occurs when the x component is advanced $\frac{\pi}{2}$ in phase with respect to the other component. We also represent our basis vectors from x, y axes as the sum of right and left circular components to represent right and left circular polarized light. The transmitted irradiance is I_3

$$I_3 = \frac{1}{\sqrt{2}}(E_x - iE_y) \frac{1}{\sqrt{2}}(E_x - iE_y)^*$$

$$= \frac{1}{2}(E_x E_x^* + E_y E_y^* + iE_x E_y^* - iE_y E_x^*)$$

Then

$$\begin{aligned} V &= 2I_3 - I_0 \\ &= (E_x E_x^* + E_y E_y^* + iE_x E_y^* - iE_y E_x^*) - (E_x E_x^* + E_y E_y^*) \\ &= i(E_x E_y^* - E_y E_x^*) \\ &= i[a_x \exp(-i\delta_x) a_y \exp(i\delta_y) - a_y \exp(-i\delta_y) a_x \exp(i\delta_x)] \\ &= i a_x a_y \{ \exp[-i(\delta_x - \delta_y)] - \exp[i(\delta_x - \delta_y)] \} \\ &= i a_x a_y (-2i \sin \delta) \\ &= 2 a_x a_y \sin \delta \end{aligned}$$

Since the four Stokes parameters are functions of the two orthogonal electric field amplitudes and the phase angle between them, they are not all independent. The Stokes parameters satisfy the relation of $I^2 \geq Q^2 + U^2 + V^2$ [3]. When light is 100% polarized, the equality holds. When the light contains an unpolarized component, the inequality holds.

2.3 Mueller Matrices

When light, represented in terms of an initial Stokes vector, passes through an optical system or scatters from a surface, a new set of Stokes vectors is needed to describe the new state of light. How can one quantitatively predict the effect of an optical device or a scatterer on the initial polarization state? The optical system can be related to a 4×4

Mueller matrix. The matrix converts one Stokes vector into another. It can be written in a mathematical form as follows

$$\begin{pmatrix} I' \\ Q' \\ U' \\ V' \end{pmatrix} = \begin{bmatrix} S_{11} & S_{12} & S_{13} & S_{14} \\ S_{21} & S_{22} & S_{23} & S_{24} \\ S_{31} & S_{32} & S_{33} & S_{34} \\ S_{41} & S_{42} & S_{43} & S_{44} \end{bmatrix} \begin{pmatrix} I \\ Q \\ U \\ V \end{pmatrix}$$

or

$$|V_{out}\rangle = [S_{ij}]|V_{in}\rangle$$

Here $[S_{ij}]$ is the Mueller matrix of the optical device, the matrix transforms Stokes vector $|V_{in}\rangle$ into the Stokes vector $|V_{out}\rangle$. Or we can say the initial beam represented by Stokes vector $|V_{in}\rangle$ is converted to $|V_{out}\rangle$ by a scattering matrix $[S_{ij}]$

$$I' = S_{11}I + S_{12}Q + S_{13}U + S_{14}V$$

$$Q' = S_{21}I + S_{22}Q + S_{23}U + S_{24}V$$

$$U' = S_{31}I + S_{32}Q + S_{33}U + S_{34}V$$

$$V' = S_{41}I + S_{42}Q + S_{43}U + S_{44}V$$

In the general case, each final polarization state can be a mixture of the initial polarization states, each weighted by the appropriate Mueller matrix element. The $[S_{ij}]$ is related to the efficiency of converting one polarization state to another or the effectiveness of the scattering interaction to cause depolarization. Each element is then a measure of how much of a particular input component is converted by the scatterer into a particular

output component as a function of the scattering angle θ . For example, matrix element $S_{12}(\theta)$ describes how much of the incident horizontal polarized light is converted as a total intensity unpolarized light as a function of θ . The elements of the first column in $[S_{ij}]$ are called total intensity matrix elements which represent total intensity only. All other matrix elements are called polarization matrix elements which relate the polarization input and output polarization. Moreover, the $[S_{ij}]$ contain information about the shape and the symmetry of the scatterer. Each element is a function of scattering angle θ . If the scatterer has spherical symmetry, cylindrical symmetry or an isotropic symmetric scatterer with mirror symmetry, not all of the elements will be independent. Some could be zero, some equal to others or differ by a negative sign. The general form of the scattering matrix is given by Van de Hulst[4].

For example, a $+45^\circ$ linear polarizer can be represented by an $[S_{ij}]$ to describe this optical device.

(a) $[S_{ij}]$ will convert the unpolarized light into a 45° polarized light with $\frac{1}{2}$ of the incident irradiance.

$$|V_{out}\rangle = [S_{ij}]|V_{in}\rangle$$

$$\frac{1}{2} \begin{pmatrix} 1 \\ 0 \\ 1 \\ 0 \end{pmatrix} = \begin{bmatrix} S_{11} & S_{12} & S_{13} & S_{14} \\ S_{21} & S_{22} & S_{23} & S_{24} \\ S_{31} & S_{32} & S_{33} & S_{34} \\ S_{41} & S_{42} & S_{43} & S_{44} \end{bmatrix} \begin{pmatrix} 1 \\ 0 \\ 0 \\ 0 \end{pmatrix}$$

$$= \begin{vmatrix} S_{11} \\ S_{21} \\ S_{31} \\ S_{41} \end{vmatrix}$$

From comparison of the first and third part of this equation, we could have

$$S_{11} = S_{31} = \frac{1}{2} \text{ and } S_{21} = S_{41} = 0$$

(b) $[S_{ij}]$ will convert the horizontal polarized light into a 45° polarized light with $\frac{1}{2}$ of the incident irradiance.

$$\frac{1}{2} \begin{vmatrix} 1 \\ 0 \\ 1 \\ 0 \end{vmatrix} = \begin{bmatrix} \frac{1}{2} & S_{12} & S_{13} & S_{14} \\ 0 & S_{22} & S_{23} & S_{24} \\ \frac{1}{2} & S_{32} & S_{33} & S_{34} \\ 0 & S_{42} & S_{43} & S_{44} \end{bmatrix} \begin{vmatrix} 1 \\ 1 \\ 0 \\ 0 \end{vmatrix}$$

$$= \begin{vmatrix} \frac{1}{2} + S_{12} \\ S_{22} \\ \frac{1}{2} + S_{32} \\ S_{42} \end{vmatrix}$$

From comparison of the first and third part of this equation, we could have

$$S_{12} = S_{22} = S_{32} = S_{42} = 0$$

(c) $[S_{ij}]$ will let all the 45° polarized light transmit.

$$\begin{aligned} \begin{vmatrix} 1 \\ 0 \\ 1 \\ 0 \end{vmatrix} &= \begin{bmatrix} \frac{1}{2} & 0 & S_{13} & S_{14} \\ 0 & 0 & S_{23} & S_{24} \\ \frac{1}{2} & 0 & S_{33} & S_{34} \\ 0 & 0 & S_{43} & S_{44} \end{bmatrix} \begin{vmatrix} 1 \\ 0 \\ 1 \\ 0 \end{vmatrix} \\ &= \begin{vmatrix} \frac{1}{2} + S_{13} \\ S_{23} \\ \frac{1}{2} + S_{33} \\ S_{43} \end{vmatrix} \end{aligned}$$

From comparison of the first and third part of this equation, we could have

$$S_{13} = S_{33} = \frac{1}{2} \text{ and } S_{23} = S_{43} = 0$$

(d) $[S_{ij}]$ will convert the right-hand circular polarized light into a 45° polarized light with $\frac{1}{2}$ of the incident irradiance.

$$\begin{aligned} \frac{1}{2} \begin{vmatrix} 1 \\ 0 \\ 1 \\ 0 \end{vmatrix} &= \begin{bmatrix} \frac{1}{2} & 0 & \frac{1}{2} & S_{14} \\ 0 & 0 & 0 & S_{24} \\ \frac{1}{2} & 0 & \frac{1}{2} & S_{34} \\ 0 & 0 & 0 & S_{44} \end{bmatrix} \begin{vmatrix} 1 \\ 0 \\ 1 \\ 0 \end{vmatrix} \\ &= \begin{vmatrix} \frac{1}{2} + S_{14} \\ S_{24} \\ \frac{1}{2} + S_{34} \\ S_{44} \end{vmatrix} \end{aligned}$$

Again, by comparing of the first and third part of this equation, we could have

$$S_{14} = S_{24} = S_{34} = S_{44} = 0$$

From the calculation above, the Mueller matrix of the 45° linear polarizer can be written as

$$[S_{ij}] = \frac{1}{2} \begin{bmatrix} 1 & 0 & 1 & 0 \\ 0 & 0 & 0 & 0 \\ 1 & 0 & 1 & 0 \\ 0 & 0 & 0 & 0 \end{bmatrix}$$

Experimentally, each matrix element for the scatterer will have a value depending on the scattering angle θ and will be represented by θ -dependent intensity curve. General speaking, there are two ways the Mueller matrix - Stokes vector technique is used to study scatterers. One is called the direct problem and the other is the inverse problem. Theory can predict the Mueller matrix elements for a given particle of specified shape, size, and composition which is illuminated by a beam of specified irradiance, polarization, and wavelength. This is so called direct problem. Experimentalists can measure the Mueller matrix elements of any scatterer. These are then used to try to predict the geometry and optical constants of the scatterer, this is the so-called inverse problem. Bohren and Huffman mentioned these examples in their book where they showed that determining the tracks made by a given dragon is an easy problem - the direct problem. Whereas determining the shape of a dragon from given tracks is a hard problem - this is the inverse problem [5].

CHAPTER 3

REFLECTION AND REFRACTION OF ELECTROMAGNETIC WAVES

In general, the metals are the best reflectors, a fact which is related to their ability to conduct electricity, and possess high absorption. Here, we start with the simpler case of reflection and refraction of electromagnetic waves at a plane interface between a nonconducting dielectric. The very basic phenomenon of reflection and refraction of light is investigated from the standard point of electromagnetic theory.

3.1 Reflection and Refraction at Surface of a Non-absorbing Medium

Consider a plane harmonic wave incident upon a plane boundary separating two different optical media. There will be reflected and transmitted waves. The medium above and below the boundary plane $z = 0$ has permeability and dielectric constant μ, ϵ and μ', ϵ' respectively. Therefore, the indices of refraction are $n = \sqrt{\mu\epsilon}$ and $n' = \sqrt{\mu'\epsilon'}$. A plane wave with a wave vector \vec{K} and frequency ω is incident from medium μ, ϵ . The refracted and reflected waves have wave vectors \vec{K}' and \vec{K}'' respectively and \vec{n} is a unit normal directed from medium μ, ϵ into medium μ', ϵ' . See Figure 3.1 for more detail.

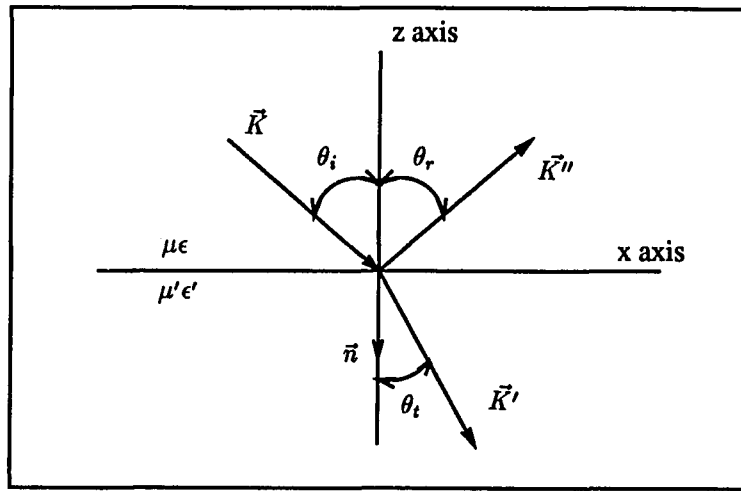


Figure 3.1: Incident wave \vec{K} strikes plane interface between two different media, giving rise to a refracted wave \vec{K}' and a reflected \vec{K}'' .

Incident wave

$$\vec{E} = \vec{E}_0 \exp i(\vec{K} \cdot \vec{r} - \omega t)$$

$$\vec{B} = \sqrt{\mu\epsilon} \frac{\vec{K} \times \vec{E}}{K}$$

Refracted (Transmitted) wave

$$\vec{E}' = \vec{E}'_0 \exp i(\vec{K}' \cdot \vec{r} - \omega t)$$

$$\vec{B}' = \sqrt{\mu'\epsilon'} \frac{\vec{K}' \times \vec{E}'}{K'}$$

Reflected wave

$$\vec{E}'' = \vec{E}''_0 \exp i(\vec{K}'' \cdot \vec{r} - \omega t)$$

$$\vec{B}'' = \sqrt{\mu\epsilon} \frac{\vec{K}'' \times \vec{E}''}{K''}$$

Boundary conditions at $z = 0$ must be satisfied at all points on the plane all the time. Therefore, the spatial and time variation of all fields must be the same at $z = 0$. Consequently, we must have the phase factors all equal at $z = 0$.

$$(\vec{K} \cdot \vec{r})_{z=0} = (\vec{K}' \cdot \vec{r})_{z=0} = (\vec{K}'' \cdot \vec{r})_{z=0}$$

These equations imply that all three wave vectors \vec{K} , \vec{K}' , and \vec{K}'' must lie in a plane and that their projection onto the boundary plane are all equal. Then we will have

$$K \sin \theta_i = K' \sin \theta_t = K'' \sin \theta_r \quad (3.1)$$

Since the space containing the incident and reflected wave ($z > 0$) is the same medium, the wave vectors have same magnitude; that is, $K = K''$. The first part and third part of Equation 3.1 then reduce to the familiar law of reflection

$$\theta_i = \theta_r$$

The angle of incidence equals the angle of reflection. The other parts of Equation 3.1 are equivalent to Snell's law

$$\frac{\sin \theta_i}{\sin \theta_t} = \frac{K}{K'} = \frac{\sqrt{\mu' \epsilon' \frac{\omega}{c}}}{\sqrt{\mu \epsilon \frac{\omega}{c}}} = \frac{n'}{n} \quad (3.2)$$

Now apply the well-known boundary conditions which require that the normal components of \vec{D} and \vec{B} and the tangential components of \vec{E} and \vec{H} be continuous. In terms of the incident, reflected, and transmitted field, these boundary condition at $z = 0$ are

$$[\epsilon(\vec{E} + \vec{E}') - \epsilon' \vec{E}'_0] \cdot \vec{n} = 0 \quad (3.3)$$

$$(\vec{K} \times \vec{E}_0 + \vec{K}'' \times \vec{E}''_0 - \vec{K}' \times \vec{E}'_0) \cdot \vec{n} = 0 \quad (3.4)$$

$$(\vec{E}_0 + \vec{E}''_0 - \vec{E}'_0) \times \vec{n} = 0 \quad (3.5)$$

$$\left[\frac{1}{\mu} (\vec{K} \times \vec{E}_0 + \vec{K}'' \times \vec{E}_0'') - \frac{1}{\mu'} (\vec{K}' \times \vec{E}_0') \right] \times \vec{n} = 0 \quad (3.6)$$

It is convenient to consider two different cases as suggested by Jackson[3]. The first case is that in which the electric vector of incident wave is parallel to the boundary plane; that is, the incident plane wave is linear polarized with polarization vector perpendicular to the plane of incidence. The case is called transverse electric or TE polarization, which is shown in Figure 3.2. The second case is that in which the magnetic vector of the incident wave is parallel to the boundary plane; that is, the polarization vector is parallel to the plane of incidence. This is called transverse magnetic or TM polarization, which is shown in Figure 3.3. The arbitrary elliptical polarization can be obtained by an appropriate linear combination of these two results. Since the electric and magnetic fields are transverse waves, the vectors can be decomposed into the electric field components parallel and perpendicular to the interface. The four boundary equations will then have two unique equations for each field component at each interface.

1. TE polarization

We first consider the electric field perpendicular to the plane of incidence as shown in Figure 3.2. Then, the Equations 3.3, 3.4, 3.5 and 3.6 reduce to two boundary equations.

$$E_0 + E_0'' - E_0' = 0$$

$$\sqrt{\frac{\epsilon}{\mu}} (E_0 - E_0'') \cos \theta_i - \sqrt{\frac{\epsilon'}{\mu'}} E_0' \cos \theta_t = 0$$

By making two assumptions, these two equations can be solved for the ratio of transmitted and reflected electric fields to the incident electric field. The first assumption is that the media are non-magnetic, so $\mu = \mu'$ allowing us to replace $\sqrt{\mu\epsilon}$

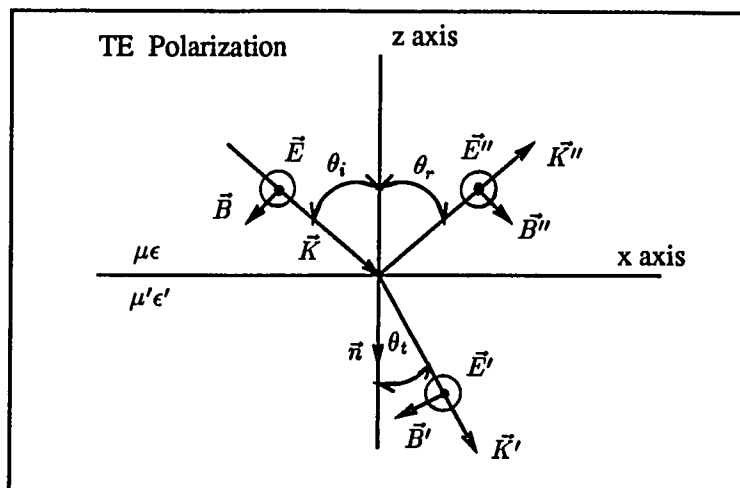


Figure 3.2: Electric field perpendicular to the plane of incidence.

and $\sqrt{\mu'\epsilon'}$ with the complex reflective index n and n' . The second assumption is no coupling between the parallel and perpendicular components. The coefficient of transmission t_{\perp} and coefficient of reflection r_{\perp} are defined as the amplitude ratio of the transmitted (refracted) beam and the reflected beam with the incident beam respectively.

$$t_{\perp} = \left(\frac{E'_0}{E_0} \right)_{TE} = \frac{2n \cos \theta_i}{n \cos \theta_i + n' \cos \theta_t} \quad (3.7)$$

$$r_{\perp} = \left(\frac{E''_0}{E_0} \right)_{TE} = \frac{n \cos \theta_i - n' \cos \theta_t}{n \cos \theta_i + n' \cos \theta_t} \quad (3.8)$$

where, using Snell's law from Equation 3.2 $\cos \theta_t$ is given by

$$\cos \theta_t = (n'^2 - n^2 \sin^2 \theta_i)^{\frac{1}{2}} n'$$

2. TM polarization

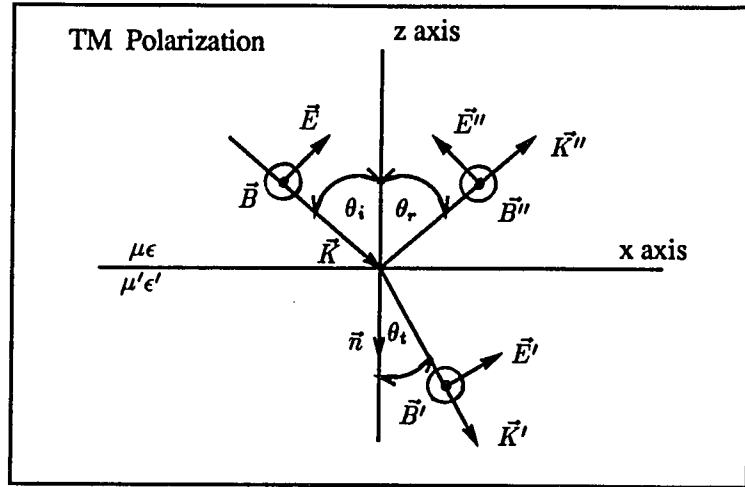


Figure 3.3: Electric field parallel to the plane of incidence.

If the electric field is parallel to the plane of incidence as shown in Figure 3.3; the boundary conditions Equation 3.3 , 3.4, 3.5, and 3.6 require that the tangential E and H be continuous therefore

$$\cos \theta_i (E_0 - E''_0) - \cos \theta_t E'_0 = 0$$

$$\sqrt{\frac{\epsilon}{\mu}} (E_0 + E''_0) - \sqrt{\frac{\epsilon'}{\mu'}} E'_0 = 0$$

Then the equations can be solved giving transmission and reflection coefficients

$$t_{\parallel} = \left(\frac{E'_0}{E_0} \right)_{TM} = \frac{2n \cos \theta_i}{n' \cos \theta_i + n \cos \theta_t} \quad (3.9)$$

$$r_{\parallel} = \left(\frac{E''_0}{E_0} \right)_{TM} = \frac{n' \cos \theta_i - n \cos \theta_t}{n' \cos \theta_i + n \cos \theta_t} \quad (3.10)$$

These Equations 3.7, 3.8, 3.9, and 3.10 are the well-known Fresnel's equations. r_{\perp} and r_{\parallel} are known as the Fresnel reflection coefficients. t_{\perp} and t_{\parallel} are known as the Fresnel transmission coefficients.

The density of the energy flux of an electromagnetic field is represented by the Poynting vector \vec{S}

$$\begin{aligned}\vec{S} &= \frac{c}{4\pi}(\vec{E} \times \vec{H}) \\ &= \frac{c}{4\pi}n|\vec{E}|^2\end{aligned}$$

The reflectances are defined as the ratios of reflected to incident energies

$$\begin{aligned}R_{\perp} &= \left(\frac{|\vec{S}'_{\perp}|}{|\vec{S}|}\right)_{TE} = \left(\frac{E''_{\perp}}{E_0}\right)_{TE}^2 = r_{\perp}^2 \\ R_{\parallel} &= \left(\frac{|\vec{S}'_{\parallel}|}{|\vec{S}|}\right)_{TM} = \left(\frac{E''_{\parallel}}{E_0}\right)_{TM}^2 = r_{\parallel}^2\end{aligned}$$

The transmittances are given by

$$\begin{aligned}T_{\perp} &= \left(\frac{|\vec{S}'_{\perp}|}{|\vec{S}|}\right)_{TE} = \frac{n'}{n} \left(\frac{E'_{\perp}}{E_0}\right)_{TE}^2 = \frac{n'}{n} t_{\perp}^2 \\ T_{\parallel} &= \left(\frac{|\vec{S}'_{\parallel}|}{|\vec{S}|}\right)_{TM} = \frac{n'}{n} \left(\frac{E'_{\parallel}}{E_0}\right)_{TM}^2 = \frac{n'}{n} t_{\parallel}^2\end{aligned}$$

For normal incidence on an isotropic medium, the reflection and transmission coefficients can be expressed in term of the index of refraction

$$\begin{aligned}R_{\perp} &= R_{\parallel} = \left(\frac{n-n'}{n+n'}\right)^2 \\ T_{\perp} &= T_{\parallel} = \frac{4nn'}{(n+n')^2}\end{aligned}$$

3.2 Reflection at the Surface of an Absorbing Medium

For the case of an absorbing medium, we need to replace the real refractive index n' by $n' - ik'$ from Snell's law Equation 3.2

$$\sin \theta_t = \frac{n \sin \theta_i}{n' - ik'}$$

Now $\sin \theta_t$ is complex and therefore does not represent the angle of refraction except for the special case $\theta_i = \theta_t = 0$. For this special case, the Fresnel reflection coefficients can

be easily found

$$r_{\perp} = r_{\parallel} = \frac{n - (n' - ik')}{n + (n' - ik')}$$

which gives for the reflectance of the surface

$$R_{\perp} = R_{\parallel} = \frac{(n - n')^2 + k'^2}{(n + n')^2 + k'^2}$$

For the case other than normal incident expressions, the reflectance expressions are cumbersome, and approximations are used. Max Born[11] discussed in the detail the types of approximations which are useful in this problem. For many absorbing materials, particularly in visible region, the wavelength is from 3800Å to 7800Å, and we have $n'^2 + k'^2 \geq 1$. With this approximation the reflectance reduces to [12]

$$\begin{aligned} R_{\perp} &= \frac{(n'^2 + k'^2) - 2n' \cos \theta_i + \cos^2 \theta_i}{(n'^2 + k'^2) + 2n' \cos \theta_i + \cos^2 \theta_i} \\ R_{\parallel} &= \frac{(n'^2 + k'^2) \cos^2 \theta_i - 2n' \cos \theta_i + 1}{(n'^2 + k'^2) \cos^2 \theta_i + 2n' \cos \theta_i + 1} \end{aligned}$$

The Fresnel transmission coefficients have no direct significance for the wave entering the absorbing medium since the attenuation of the wave is severe and depends on the distance traveled in the medium.

3.3 Diffuse Reflection

The first law of diffuse reflection was introduced by Lambert (1760) on the basis of the observation that a white wall illuminated by sunlight appears equally bright at all observation angles. He assumed that such a surface behaves as though it itself were radiating independent of the angle of incidence of radiation. Kortüm (1969)[13] considered

the diffuse surface of a solid uniformly irradiated by parallel beam of light at angle of incidence θ_i . Then the radiation flux per unit surface area is

$$\frac{dI_i}{df} = S_0 \cos \theta_i$$

where S_0 is the irradiation intensity for normal incidence. The remitted radiation flux per unit surface area of the irradiated surface is

$$\frac{dI_r}{df} = B \cos \theta \, d\omega \quad (3.11)$$

where B is the proportionality factor called the radiation density (surface brightness). θ is the angle at which the radiating surface is observed and $d\omega$ is the solid angle. The total reemitted radiation strength is then

$$\int_{\Omega} B \cos \theta \, d\omega = \int_0^{\frac{\pi}{2}} \int_0^{2\pi} B \cos \theta \sin \theta \, d\theta \, d\varphi = \pi B$$

since the incoming and outgoing radiation intensity must be proportional to each other

$$\begin{aligned} C S_0 \cos \theta_i &= \pi B \\ \text{or } B &= \frac{C}{\pi} S_0 \cos \theta_i \end{aligned} \quad (3.12)$$

Here C is a constant. From Equations 3.11 and 3.12, the reemitted radiation flux per unit area and solid angle is

$$\frac{dI_r/df}{d\omega} = B \cos \theta = \frac{C}{\pi} S_0 \cos \theta_i \cos \theta$$

This is proportional to the cosine of the incident angle θ_i and to the cosine of the angle of the observation θ . This is known as Lambert cosine law. In this law, the constant C gives the fraction of the incident radiation flux which is reemitted, and is always less

than 1. Some portion of the radiation is always absorbed. Generally, deviations from the Lambert law are always found so there is no such thing as an “ideal diffuse reflector” in real life.

3.4 The Relation Between Fresnel Coefficients and Scattering Matrix Elements

One goal of this work was to put the Fresnel coefficients (for reflection) into the Mueller matrix - Stokes vector context (for scattering). The nephelometer measures the four Mueller matrix elements S_{11} , S_{12} , S_{33} , and S_{34} for a smooth non-absorbing coated surface. These elements can be defined in terms of the electric fields. Using the transformation matrix [5]

$$\begin{pmatrix} E_{\parallel s} \\ E_{\perp s} \end{pmatrix} = \frac{\exp ik(r-z)}{-ikr} \begin{pmatrix} S_2 & S_3 \\ S_4 & S_1 \end{pmatrix} \begin{pmatrix} E_{\parallel i} \\ E_{\perp i} \end{pmatrix}$$

Where the S_j ($j=1,2,3,4$) are amplitude scattering matrix elements. S_1 is the perpendicular component and S_2 is the parallel component of the electric field under reflection and transmission. The S_3 and S_4 elements are zero, since the media are not optically active. Therefore, the four Mueller matrix elements can be given via Fresnel equations [5]

$$\begin{aligned} S_{11} &= \frac{1}{2} (|S_1|^2 + |S_2|^2) & S_{12} &= \frac{1}{2} (|S_2|^2 - |S_1|^2) \\ S_{33} &= \text{Real} (S_1 S_2^*) & S_{34} &= \text{Imaginary} (S_2 S_1^*) \end{aligned}$$

The total intensity matrix element, S_{11} , is the average of intensity of the two electric field components. The other three elements show ratios of the various polarizations. Especially, for non-absorbing media, S_{34} is always zero.

CHAPTER 4

NEPHELOMETER TECHNIQUE

The instrument was used in this work is called a nephelometer. It can be used to study different types of scatterers by using various optical elements, electronic sampling, and laser-detector techniques. The schematic diagram of the nephelometer is shown in Figure 4.1. We have known that the Stokes vector characterizes the polarization state of light and the Mueller matrix characterizes the scatterer. From this experimental setup, the Mueller matrix elements S_{ij} can be experimentally determined. The complete design and operation can be found in Hunt and Huffman (1973)[6], Bickel et al. (1976)[7], Bell (1981)[8], and Iafelice (1985)[9].

The light source was a 16 mW He-Cd laser (441.6 nm). The incoming beam passes through a variable neutral density filter which can be used to control the intensity of the beam. It then passes through a spatial filter which is used to adjust the laser beam profile and spot size. A linear polarizer-photoelastic modulator combination is used to set the polarization of the input beam. Before the laser beam illuminates the sample, it passes through a pinhole aperture which serves as a spatial filter. After the beam goes through the filter and polarizer it is not only of the highest quality but it is also in the desired polarization state.

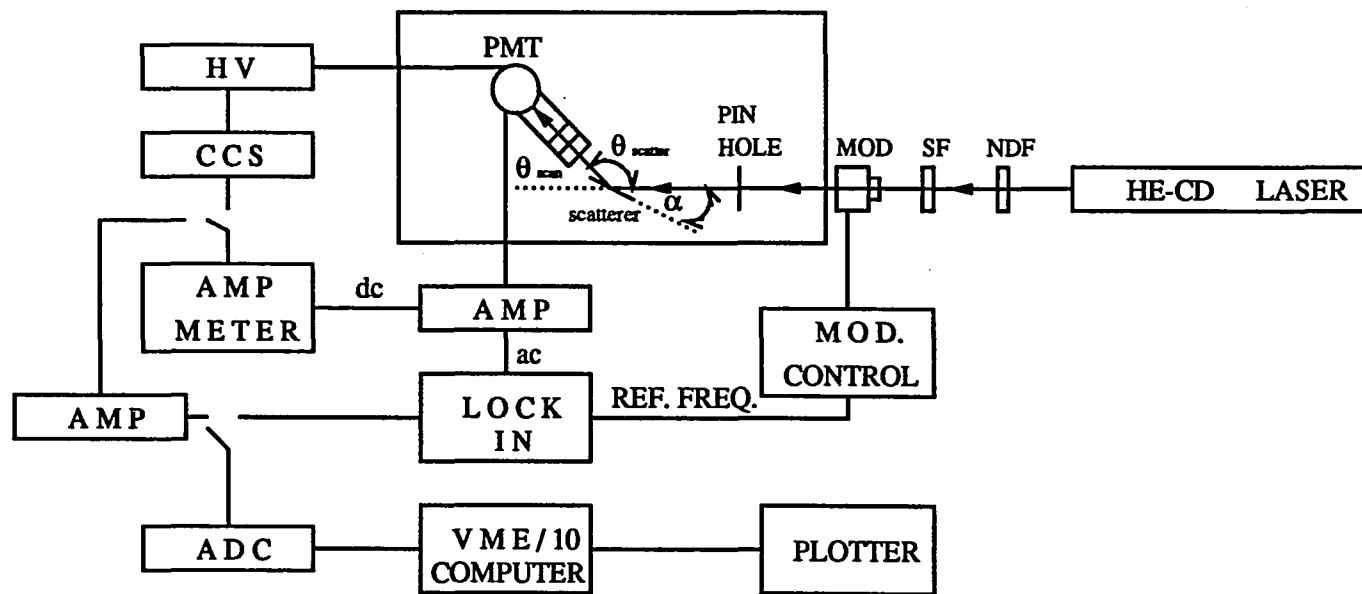


Figure 4.1: Schematic diagram of nephelometer setup.

A platform which consists of an x, y, z translator, tilt positioner, and a rotational mount is used to hold the sample holder so that the sample could be placed at the exact rotation center of the detector. The samples under investigation were mounted on a black painted holder to prevent unnecessary scattering from the holder. Generally, the scattered light from a sample goes into all space. Some of the light scattered by the sample is detected by a photomultiplier tube, which is mounted on a rectangular arm with slit, polarizer, quarter wave plate, and filter. A dc motor rotates the θ -scan arm from 0° to 170° about the sample. An exit slit, of width 0.5 mm, is placed before the PMT about 29 cm away from the slit. Therefore, the angular spread $\Delta\theta$ of the scattered light into the detector is

$$\Delta\theta = \frac{0.5mm}{29cm} \equiv 0.00172 \text{ rad} \sim 0.2^\circ$$

The PMT can be operated at any voltage up to a maximum of 1100 volts dc. For total intensity measurements, negative 600 volts was used. The dc signal from the PMT was connected to a logarithmic picoammeter (Keithley model 26000). In order to keep intensity of light in an appropriate range (above dark current and below tube saturation) the incident laser beam intensity was adjusted with neutral density filters to stay between 10^{-5} and 10^{-9} amp. The dc signal from the logarithmic picoammeter is sent to an analog to digital converter (ADC), and then to a Motorola VME/10 minicomputer for calculation, analysis, and storage. The other matrix elements are polarization signals and a different measuring technique was used. The ac component of the PMT signal was detected by a lock-in amplifier (PAR HR-8). The lock-in amplifier essentially tunes in on the frequency and amplifies the polarization carried on the modulated ac signal. The amplitude of the ac signal detected by the lock-in amplifier is proportional to the percent polarization of a

particular polarization state. During the measurement, a dc portion of PMT signal is fed to a constant current servo, which is designed to keep the PMT output current constant for a varying intensity input. A beam stop made of a black plastic tube prevented the saturation of PMT at $\theta = 0^\circ$ and during the first few degrees of the scan.

4.1 Polarization Modulation Techniques

A major technique developed by Hunt and Huffman (1973)[6] was used to determine experimentally the Muller matrix element S_{ij} . The technique uses a polarization modulated beam and lock-in detection to produce the various scattering matrix element S_{ij} . The modulator tunes in on certain harmonics and the detected signal is proportional to the matrix elements.

4.1.1 The Modulator

The birefringent piezo-elastic modulator (Morvue electronic system photoelastic modulator PEM-3) is a block of amorphous quartz which is driven at its 50K Hz natural frequency by a piece of crystalline quartz of similar properties. The modulator is aligned with its face perpendicular to the laser beam and its long dimension parallel to the scattering plane. The orientation of the linear polarizer and modulator is fixed as a unit. The incoming light passes through the polarizer first and then goes through the modulator. The light input to the modulator is prepared to be linearly polarized 45° with respect to the modulator axis in order to modify the state of incoming light. The amplitude of the oscillator circuit is adjustable to select the applied stress which squeezes or compresses the

amorphous quartz. This phenomenon induces a periodic birefringence of the quartz. The changing of index of refraction n modifies the polarization state of the incoming light from linear to alternately right and left circular polarized light, depending on the modulator axis.

For example, when the modulator axis is at 90° , the 45° polarizer will create a 45° polarized light for the modulator. This polarized light can be represented by two components of the electric field $E_x = E_{0x} \sin \frac{2\pi z}{\lambda}$ and $E_y = E_{0y} \sin \frac{2\pi z}{\lambda}$. Each component enters the modulator in phase but travels through the modulator at different speed depending on the index of refraction n_x and n_y for each component. When the modulator is squeezed or extended a phase shift of one component will occur. The amplitude of the modulator can be adjusted to create exactly a $\frac{\lambda}{4}$ (90°) phase shift between these two components. At one extreme, when the modulator is compressed and the amplitude is adjusted properly so that $n_x > n_y$, the x component will travel slower in the modulator than the y component. The x component will be retarded by exactly $\frac{\lambda}{4}$ by the time it leaves the modulator. The rotation of the resultant E vector is counterclockwise (left-circular) as seen for the wave coming at you. At the other extreme when the modulator is extended so that $n_x < n_y$, the y component will be retarded exactly by $\frac{\lambda}{4}$. A right-circular light will be formed. When the modulator is relaxed, $n_x = n_y$, no phase shift occurs and the modulator passes the 45° linear polarized light through unaltered. Between the points where the modulator is compressed and relaxed the elliptical polarization state occurs where the major axis is tilted by 45° .

The rapidly changing indices of n_x and n_y in the modulator essentially causes the slab of quartz to act as a sinusoidally varying phase plate. Consider the phase retardation varying with time [10];

$$\begin{aligned}\delta(t) &= \frac{2\pi d}{\lambda} s \sin \omega t \\ &= A \sin \omega t\end{aligned}$$

where

d = thickness of the modulator element

λ = wavelength of transmitted light

s = stress coefficient

ω = resonant frequency of the slab (50K Hz)

Since the phase retarder causes the time-dependent polarization of the incident beam, the signal of the scattered light will contain harmonics which are proportional to different input polarizations. When the input light is described by the Stokes vector $|V_{in}|$, the emerging light $|V_{out}|$ can be found by the product of the Mueller matrices of the all optical elements with the input Stokes vectors.

$$|V_{out}| = [S_n] \cdots [S_2][S_1]|V_{in}|$$

In the experimental setup, two combinations of linear polarizer and modulator are used. One is : polarizer at 45° and modulator fast axis at 90° ; the other is : polarizer at 0° and modulator fast axis at 45° . In these two cases, the relative angle between the input polarizer and modulator is 45° .

Consider the arrangement given by case I. The initial linear polarizer is at 45° with the modulator fast axis at 90° . The Stokes vector of the unpolarized incoming light is given by

$$\begin{bmatrix} 1 \\ 0 \\ 0 \\ 0 \end{bmatrix}$$

The Mueller matrix for an 45° ideal homogeneous linear polarizer is

$$\frac{1}{2} \begin{bmatrix} 1 & 0 & 1 & 0 \\ 0 & 0 & 0 & 0 \\ 1 & 0 & 1 & 0 \\ 0 & 0 & 0 & 0 \end{bmatrix}$$

The Mueller matrix for an ideal homogeneous linear retarder with fast axis at 90° is

$$[M_{90^\circ}] = \begin{bmatrix} 1 & 0 & 0 & 0 \\ 0 & 1 & 0 & 0 \\ 0 & 0 & \cos \delta & -\sin \delta \\ 0 & 0 & \sin \delta & \cos \delta \end{bmatrix}$$

where δ is the angle of retardation. The Stokes vector representing the light as it emerges from the modulator is given by the matrix product

$$\frac{1}{2} \begin{bmatrix} 1 & 0 & 0 & 0 \\ 0 & 1 & 0 & 0 \\ 0 & 0 & \cos \delta & -\sin \delta \\ 0 & 0 & \sin \delta & \cos \delta \end{bmatrix} \begin{bmatrix} 1 & 0 & 1 & 0 \\ 0 & 0 & 0 & 0 \\ 1 & 0 & 1 & 0 \\ 0 & 0 & 0 & 0 \end{bmatrix} \begin{bmatrix} 1 \\ 0 \\ 0 \\ 0 \end{bmatrix} = \frac{1}{2} \begin{bmatrix} 1 \\ 0 \\ \cos \delta \\ \sin \delta \end{bmatrix}$$

The scattering from a scatterer is given by the scattering Mueller matrix operation on above Stokes vector

$$\frac{1}{2} \begin{bmatrix} S_{11} & S_{12} & S_{13} & S_{14} \\ S_{21} & S_{22} & S_{23} & S_{24} \\ S_{31} & S_{32} & S_{33} & S_{34} \\ S_{41} & S_{42} & S_{43} & S_{44} \end{bmatrix} \begin{bmatrix} 1 \\ 0 \\ \cos \delta \\ \sin \delta \end{bmatrix} = \frac{1}{2} \begin{bmatrix} S_{11} + S_{13} \cos \delta + S_{14} \sin \delta \\ S_{21} + S_{23} \cos \delta + S_{24} \sin \delta \\ S_{31} + S_{33} \cos \delta + S_{34} \sin \delta \\ S_{41} + S_{43} \cos \delta + S_{44} \sin \delta \end{bmatrix}$$

(a) If there is no further polarizer in the light path, the photomultiplier will response to the total intensity of light which is the first element of Stokes vector,

$$I_{det} = \frac{k}{2}(S_{11} + S_{13} \cos \delta + S_{14} \sin \delta)$$

where k is a constant depending on the phototube sensitivity, light collecting efficiency etc.

If there are further polarizers used for the analysis of the polarization state before it enter the detector, we calculate the Stokes vector emerging from the final ideal homogeneous linear polarizer as follows :

$$\frac{1}{4} \begin{bmatrix} 1 & \cos 2\theta & \sin 2\theta & 0 \\ \cos 2\theta & \cos^2 2\theta & \cos 2\theta \sin 2\theta & 0 \\ \sin 2\theta & \cos 2\theta \sin 2\theta & \sin^2 2\theta & 0 \\ 0 & 0 & 0 & 0 \end{bmatrix} \begin{bmatrix} S_{11} + S_{13} \cos \delta + S_{14} \sin \delta \\ S_{21} + S_{23} \cos \delta + S_{24} \sin \delta \\ S_{31} + S_{33} \cos \delta + S_{34} \sin \delta \\ S_{41} + S_{43} \cos \delta + S_{44} \sin \delta \end{bmatrix} = \frac{1}{4} \begin{bmatrix} I' \\ Q' \\ U' \\ V' \end{bmatrix}$$

where

θ = the angle of polarizer

$$I' = (S_{11} + S_{21} \cos 2\theta + S_{31} \sin 2\theta) + (S_{13} + S_{23} \cos 2\theta + S_{33} \sin 2\theta) \cos \delta$$

$$\begin{aligned}
& +(S_{14} + S_{24} \cos 2\theta + S_{34} \sin 2\theta) \sin \delta \\
Q' &= (S_{11} \cos 2\theta + S_{21} \cos^2 2\theta + S_{31} \cos 2\theta \sin 2\theta) \\
& +(S_{13} \cos 2\theta + S_{23} \cos^2 2\theta + S_{33} \cos 2\theta \sin 2\theta) \cos \delta \\
& +(S_{14} \cos 2\theta + S_{24} \cos^2 2\theta + S_{34} \cos 2\theta \sin 2\theta) \sin \delta \\
U' &= (S_{11} \sin 2\theta + S_{21} \cos 2\theta \sin 2\theta + S_{31} \sin^2 2\theta) \\
& +(S_{13} \sin 2\theta + S_{23} \cos 2\theta \sin 2\theta + S_{33} \sin^2 2\theta) \cos \delta \\
& +(S_{14} \sin 2\theta + S_{24} \cos 2\theta \sin 2\theta + S_{34} \sin^2 2\theta) \sin \delta \\
V' &= 0
\end{aligned}$$

(b) If we use a horizontal linear polarizer ($\theta = 0^\circ$), The Stokes vector will be

$$\begin{aligned}
& \frac{1}{4} \begin{bmatrix} 1 & 1 & 0 & 0 \\ 1 & 1 & 0 & 0 \\ 0 & 0 & 0 & 0 \\ 0 & 0 & 0 & 0 \end{bmatrix} \begin{vmatrix} S_{11} + S_{13} \cos \delta + S_{14} \sin \delta \\ S_{21} + S_{23} \cos \delta + S_{24} \sin \delta \\ S_{31} + S_{33} \cos \delta + S_{34} \sin \delta \\ S_{41} + S_{43} \cos \delta + S_{44} \sin \delta \end{vmatrix} \\
&= \frac{1}{4} \begin{vmatrix} (S_{11} + S_{21}) + (S_{13} + S_{23}) \cos \delta + (S_{14} + S_{24}) \sin \delta \\ (S_{11} + S_{21}) + (S_{13} + S_{23}) \cos \delta + (S_{14} + S_{24}) \sin \delta \\ 0 \\ 0 \end{vmatrix}
\end{aligned}$$

The detector sees only the total intensity which is the first component of this vector

$$I_{det} = \frac{k}{4} [(S_{11} + S_{21}) + (S_{13} + S_{23}) \cos \delta + (S_{14} + S_{24}) \sin \delta]$$

(c) In the experiment, we use a 45° linear polarizer. The Stokes vector emerging from the final polarizer is

$$\begin{aligned}
 & \frac{1}{4} \begin{bmatrix} 1 & 0 & 1 & 0 \\ 0 & 0 & 0 & 0 \\ 1 & 0 & 1 & 0 \\ 0 & 0 & 0 & 0 \end{bmatrix} \begin{vmatrix} S_{11} + S_{13} \cos \delta + S_{14} \sin \delta \\ S_{21} + S_{23} \cos \delta + S_{24} \sin \delta \\ S_{31} + S_{33} \cos \delta + S_{34} \sin \delta \\ S_{41} + S_{43} \cos \delta + S_{44} \sin \delta \end{vmatrix} \\
 &= \frac{1}{4} \begin{vmatrix} (S_{11} + S_{31}) + (S_{13} + S_{33}) \cos \delta + (S_{14} + S_{34}) \sin \delta \\ 0 \\ (S_{11} + S_{31}) + (S_{13} + S_{33}) \cos \delta + (S_{14} + S_{34}) \sin \delta \\ 0 \end{vmatrix}
 \end{aligned}$$

The detector sees

$$I_{det} = \frac{k}{4} [(S_{11} + S_{31}) + (S_{13} + S_{33}) \cos \delta + (S_{14} + S_{34}) \sin \delta]$$

(d) If we use right-circular polarizer, the Stokes vector will be

$$\begin{aligned}
 & \frac{1}{4} \begin{bmatrix} 1 & 0 & 0 & 1 \\ 0 & 0 & 0 & 0 \\ 0 & 0 & 0 & 0 \\ 1 & 0 & 0 & 1 \end{bmatrix} \begin{vmatrix} S_{11} + S_{13} \cos \delta + S_{14} \sin \delta \\ S_{21} + S_{23} \cos \delta + S_{24} \sin \delta \\ S_{31} + S_{33} \cos \delta + S_{34} \sin \delta \\ S_{41} + S_{43} \cos \delta + S_{44} \sin \delta \end{vmatrix} \\
 &= \frac{1}{4} \begin{vmatrix} (S_{11} + S_{41}) + (S_{13} + S_{43}) \cos \delta + (S_{14} + S_{44}) \sin \delta \\ 0 \\ 0 \\ (S_{11} + S_{41}) + (S_{13} + S_{43}) \cos \delta + (S_{14} + S_{44}) \sin \delta \end{vmatrix}
 \end{aligned}$$

The detector sees

$$I_{det} = \frac{k}{4} [(S_{11} + S_{41}) + (S_{13} + S_{43}) \cos \delta + (S_{14} + S_{44}) \sin \delta]$$

For the case II, the initial linear polarizer at 0° with modulator fast axis at 45° . We use

$$\frac{1}{2} \begin{bmatrix} 1 & 1 & 0 & 0 \\ 1 & 1 & 0 & 0 \\ 0 & 0 & 0 & 0 \\ 0 & 0 & 0 & 0 \end{bmatrix}$$

as the Mueller matrix of a 0° ideal homogeneous linear polarizer and

$$[M_{45^\circ}] = \begin{bmatrix} 1 & 0 & 0 & 0 \\ 0 & \cos \delta & 0 & -\sin \delta \\ 0 & 0 & 1 & 0 \\ 0 & \sin \delta & 0 & \cos \delta \end{bmatrix}$$

as the Mueller matrix of an ideal homogeneous linear retarder with fast axis at 45° . The calculations for the intensity measured by the photomultiplier are similar to those used in case I.

4.2 Lock-in Detection and Electronic System

4.2.1 The Constant Current Servo

Since the detected signal contains a dc and two ac terms, the dc portion of photomultiplier tube signal is separated electronically and fed to a constant current servo (ccs) to control the PMT high voltage in order to keep PMT output current constant for a varying

intensity input. As I_{det} changes, PMT current i changes. The picoammeter measures the current i and generates a voltage proportional to this current. At the same time, the voltage unbalances the present value of ccs, creating another voltage, which decreases the voltage V on PMT. Decreased voltage at the PMT decreases the tube gain and reduces the current i until the ccs is balanced. Since the response is very fast ($< \text{msec}$), i can be considered remaining constant independent of I_{det} . This effectively divides the detector signal by dc component so the current from the detector in cases (a), (b), (c), and (d) are respectively

$$(a) i_a = \left(1 + \frac{S_{13}}{S_{11}} \cos \delta + \frac{S_{14}}{S_{11}} \sin \delta\right) R \quad (4.1)$$

$$(b) i_b = \left(1 + \frac{S_{13} + S_{23}}{S_{11} + S_{21}} \cos \delta + \frac{S_{14} + S_{24}}{S_{11} + S_{21}} \sin \delta\right) R \quad (4.2)$$

$$(c) i_c = \left(1 + \frac{S_{13} + S_{33}}{S_{11} + S_{31}} \cos \delta + \frac{S_{14} + S_{34}}{S_{11} + S_{31}} \sin \delta\right) R \quad (4.3)$$

$$(d) i_d = \left(1 + \frac{S_{13} + S_{43}}{S_{11} + S_{41}} \cos \delta + \frac{S_{14} + S_{44}}{S_{11} + S_{41}} \sin \delta\right) R \quad (4.4)$$

where R is the response of PMT. The ac portion of this signal goes through a preamplifier then into the lock-in amplifier which is tuned to pick out and amplify the desired harmonic.

4.2.2 Lock-in Amplifier

The phase retarder is a sinusoidal function of time. From the derivation, it occurs as an argument of the trigonometric function in the current. Expanding $\sin \delta$ and $\cos \delta$ in terms of Bessel functions,

$$\sin \delta = \sin(A \sin \omega t) = 2J_1(A) \sin \omega t + 2J_3(A) \sin 3\omega t + \dots \quad (4.5)$$

$$\cos \delta = \cos(A \cos \omega t) = J_0(A) + 2J_2(A) \cos 2\omega t + \dots \quad (4.6)$$

Insert the Equation 4.5 and 4.6 into Equation 4.1, 4.2, 4.3, and 4.4 we will have

$$(a) i_a = [1 + \frac{S_{13}}{S_{11}}J_0(A) + \frac{S_{13}}{S_{11}}2J_2(A) \cos 2\omega t + \frac{S_{14}}{S_{11}}2J_1(A) \sin \omega t + \dots]R \quad (4.7)$$

$$(b) i_b = [1 + \frac{S_{13} + S_{23}}{S_{11} + S_{21}}J_0(A) + \frac{S_{13} + S_{23}}{S_{11} + S_{21}}2J_2(A) \cos 2\omega t + \frac{S_{14} + S_{24}}{S_{11} + S_{21}}2J_1(A) \sin \omega t + \dots]R \quad (4.8)$$

$$(c) i_c = [1 + \frac{S_{13} + S_{33}}{S_{11} + S_{31}}J_0(A) + \frac{S_{13} + S_{33}}{S_{11} + S_{31}}2J_2(A) \cos 2\omega t + \frac{S_{14} + S_{34}}{S_{11} + S_{31}}2J_1(A) \sin \omega t + \dots]R \quad (4.9)$$

$$(d) i_d = [1 + \frac{S_{13} + S_{43}}{S_{11} + S_{41}}J_0(A) + \frac{S_{13} + S_{43}}{S_{11} + S_{41}}2J_2(A) \cos 2\omega t + \frac{S_{14} + S_{44}}{S_{11} + S_{41}}2J_1(A) \sin \omega t + \dots]R \quad (4.10)$$

These equations depend on the resonant frequency ω of the modulator and contain linear combinations of the matrix elements. To simplify the data interpretation, the amplitude of the vibration of the modulator is adjusted to $A = 138^\circ$ which corresponds to the first zero of the $J_0(A)$ function. With the lock-in tuned to ω (=50K Hz), from Equation 4.7 to Equation 4.10 the output is equal to the rms value of the fundamental frequency

$$(a) \frac{2}{\sqrt{2}}RJ_1(138^\circ)\frac{S_{14}}{S_{11}} = S_{14}^*$$

$$(b) \frac{2}{\sqrt{2}}RJ_1(138^\circ)\frac{S_{14} + S_{24}}{S_{11} + S_{21}} = S_{24}^*$$

$$(c) \frac{2}{\sqrt{2}}RJ_1(138^\circ)\frac{S_{14} + S_{34}}{S_{11} + S_{31}} = S_{34}^*$$

$$(d) \frac{2}{\sqrt{2}}RJ_1(138^\circ)\frac{S_{14} + S_{44}}{S_{11} + S_{41}} = S_{44}^*$$

The signal denoted as S_{ij}^* (for example $S_{23}^* = \frac{S_{13} + S_{23}}{S_{11} + S_{21}}$) because they are the actual elements extracted, when detecting the above combination of matrix elements. In the calibration procedure, we set the constant in front of each matrix element combination to unity.

When the lock-in frequency is tuned to 2ω ($=100\text{K Hz}$), Equation 4.7 to Equation 4.10 give signals :

$$\begin{aligned}
 (a) \quad & \frac{2}{\sqrt{2}} R J_2(138^\circ) \frac{S_{13}}{S_{11}} = S_{13}^* \\
 (b) \quad & \frac{2}{\sqrt{2}} R J_2(138^\circ) \frac{S_{13} + S_{23}}{S_{11} + S_{21}} = S_{23}^* \\
 (c) \quad & \frac{2}{\sqrt{2}} R J_2(138^\circ) \frac{S_{13} + S_{33}}{S_{11} + S_{31}} = S_{33}^* \\
 (d) \quad & \frac{2}{\sqrt{2}} R J_1(138^\circ) \frac{S_{13} + S_{43}}{S_{11} + S_{41}} = S_{43}^*
 \end{aligned}$$

4.3 The Experimental Matrix $S_{ij}^*(\theta)$

The orientation of the input and analyzing optics required to measure each matrix element and the required lock-in reference frequency for each measurement is shown in Figure 4.2. All the combinations of matrix elements obtained here were worked out in detail by Bell (1981)[8]. The matrix elements are measured by scanning the detector through angle θ .

4.4 Calibration

The optical orientations and lock-in frequencies needed to calibrate the nephelometer are shown in Figure 4.3. The calibration requires that the polarization component of the input light be totally converted to the output state to be measured. This makes the calibration procedure very easy. To calibrate for full scale (100%) for a particular polarization, the detector is set at 0° . We then adjust the electronics and filters to give a $\pm 100\%$ polarization swing on the lock-in when the analyzing polarizer is rotated $\pm 90^\circ$. The instrument is then calibrated to give a 100% signal when the “pure” input

S_{11} * ⁱ * 45° 90° Hole D.C.	S_{12} ↔ * ⁱ 0° 45° Hole 100 kHz	S_{13} ↗ * 45° 90° Hole 100 kHz	S_{14} ↻ * 0° 45° Hole 50 kHz
S_{21} * ↔ 45° 90° 0° D.C.	S_{22} ↔ ↔ 0° 45° 0° 100 kHz	S_{23} ↗ ↔ 45° 90° 0° 100 kHz	S_{24} ↻ ↔ 0° 45° 0° 50 kHz
S_{31} * ↗ 45° 90° 45° D.C.	S_{32} ↔ ↗ 0° 45° 45° 100 kHz	S_{33} ↗ ↗ 45° 90° 45° 100 kHz	S_{34} ↻ ↗ 0° 45° 45° 50 kHz
S_{41} * ↻ 45° 90° 0° 45° D.C.	S_{42} ↔ ↻ 0° 45° 0° 45° 100 kHz	S_{43} ↗ ↻ 45° 90° 0° 45° 100 kHz	S_{44} ↻ ↻ 0° 45° 0° 45° 50 kHz

Figure 4.2: Orientations of the optical elements required to measure S_{ij} .

S_{11}^* * * D.C.	S_{12}^* ↔ * 100 kHz	S_{13}^* ↗ * 100 kHz	S_{14}^* ↻ * 50 kHz
Set to 1 at an arbitrary angle.	↑	↑	↑
S_{21}^* * ↔	S_{22}^* ↔ ↔ 100 kHz	S_{23}^* ↗ ↔ 100 kHz	S_{24}^* ↻ ↔ 50 kHz
↓	 0° 45° 0° +100%	↑	↑
S_{31}^* * ↗	S_{32}^* ↔ ↗ 100 kHz	S_{33}^* ↗ ↗ 100 kHz	S_{34}^* ↻ ↗ 50 kHz
↓	↓	 45° 90° 45° +100%	↑
S_{41}^* * ↻	S_{42}^* ↔ ↻ 100 kHz	S_{43}^* ↗ ↻ 100 kHz	S_{44}^* ↻ ↻ 50 kHz
↓	↓	↓	 0° 45° 0° 45° +100%

Figure 4.3: Calibration orientations and lock-in frequencies to measure matrix elements.

Stokes parameter is entirely converted to the output Stokes parameter. Since the total irradiance detected is forced to be a constant by the constant current servo, the measured irradiance is always the fraction of the total irradiance in the particular Stokes parameter being analyzed. Therefore after calibration, the fraction of polarized irradiance detected divided by the total irradiance detected is equal to one. As mention before, from the relation of the $I^2 \geq Q^2 + U^2 + V^2$, the equality holds for totally polarized light and inequality holds for an unpolarized component is present or partially polarized light. The fraction of polarization can be determined by [3]

$$\pi = \frac{(Q^2 + U^2 + V^2)^{1/2}}{I}$$

Thus, a particular measurement of a Stokes parameter at some fixed angle θ yielding a signal of $\pm 100\%$ (total polarized) implies that all other Stokes parameter at this angle are equal to zero.

The calibration orientations and lock-in frequency used for the fourth column calculation are indicated by the S_{44}^* calibration example. When we set the initial polarizer 0° , the modulator fast axis to 45° , and lock-in frequency at 50K Hz, the emergent light is right-circular polarized. This circularly polarized light can be resolved into two plane polarized components which are $\frac{\pi}{2}$ out of phase. With a quarter wave plate, this phase difference can be removed. Therefore, a 45° plane polarized light emerges from the final analyzing 45° polarizer before entering the PMT. Therefore the 100% right-circular polarized light can be detected. At the same time, the modulator amplitude, ccs, and lock-in setting are adjusted to produced a full scale deflection on the lock-in. Since the ac signal is held constant by the ccs, the calibration is preserved through all scan angles

and is independent of the source intensity fluctuations. The total intensity measurements, elements in the first column, do not use the ccs and their signals vary over several orders of magnitudes. They are normalized to unity at some chosen angle after the data are transferred to the computer. After calibration for each column, the necessary output optical elements are chosen to measure the desired matrix element shown in Figure 4.2.

CHAPTER 5

SAMPLE PREPARATION

The goal of the study reported here is to examine the scattering properties of Mueller Matrix elements of samples as a function of surface roughness or index of refraction. In this method, an initial starting point will be a smooth surface whose scattering properties will change when perturbations (defects) are added to surface.

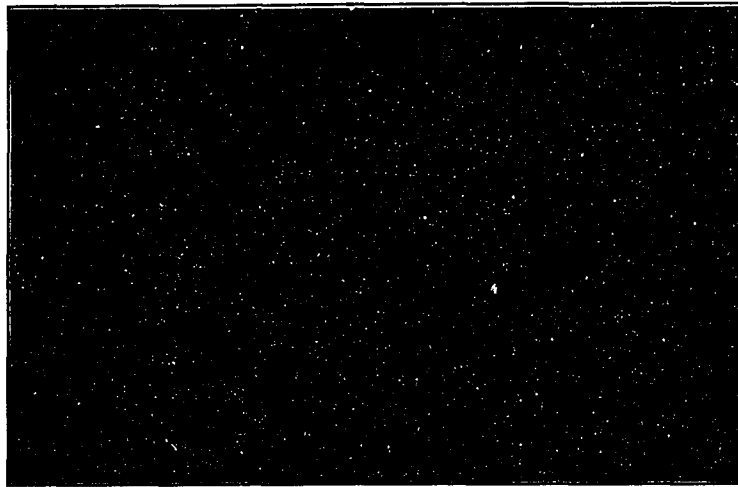
To study surface scattering, eight aluminum substrates were initially polished to create high reflectivity surfaces. Then a family of rough surfaces were created. Aluminum substrates # 1 to # 7 (they were exposed to the air and a layer of aluminum oxide was on those surfaces) were each roughened to different amounts (from zero roughness to saturation) by the method of glass sandblasting. A photograph of the glass sand is shown in Figure 5.1. Sample # 0 remained a mirror and was treated as a reference. The other seven mirrors were sandblasted to increasing the roughness by the increasing the duration of sand blasted. The rms surface roughness (σ) of the samples are shown in the Table 5.1. Micrographs of these surfaces were taken on the ISI super III- A SEM machine and are shown from Figure 5.2 to Figure 5.9. The photographs show the increasing of surface roughness.



Figure 5.1: Micrograph of the glass sand which was used to create the aluminum rough surface.

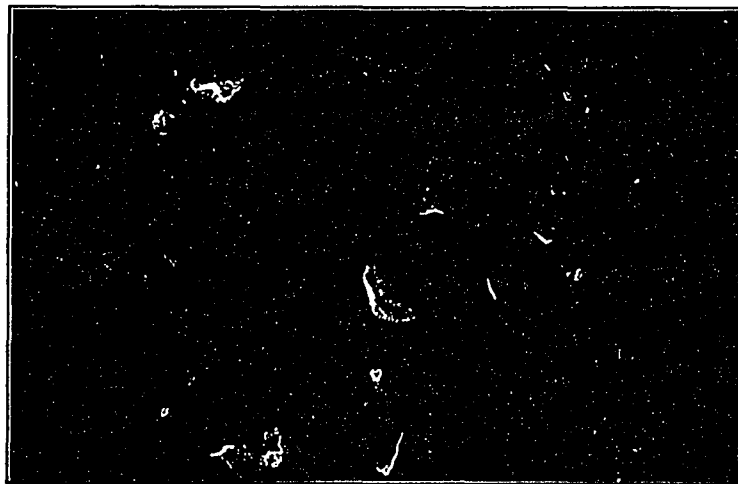
sample #	rms surface roughness σ
sample # 0	0.056 μm
sample # 1	0.371 μm
sample # 2	1.470 μm
sample # 3	1.566 μm
sample # 4	2.101 μm
sample # 5	2.700 μm
sample # 6	3.479 μm
sample # 7	3.607 μm
sample # 10	11.317 μm
sample # 11	11.090 μm

Table 5.1: Measured rms surface roughness (σ) for samples.



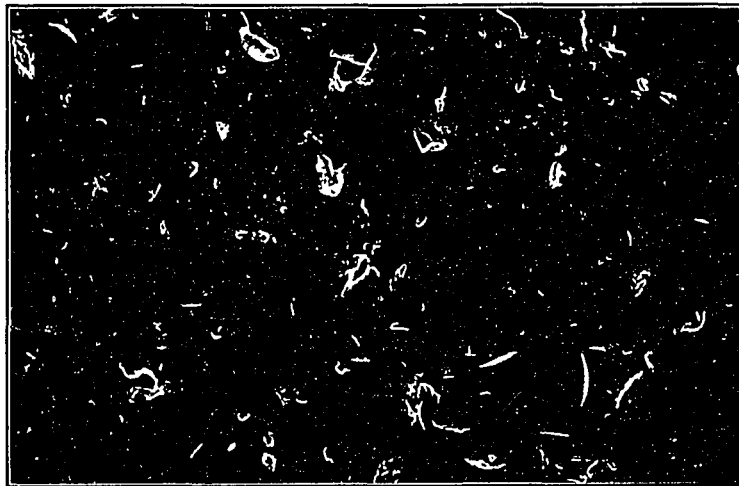
100 μm

Figure 5.2: Micrograph of smooth surface sample # 0.



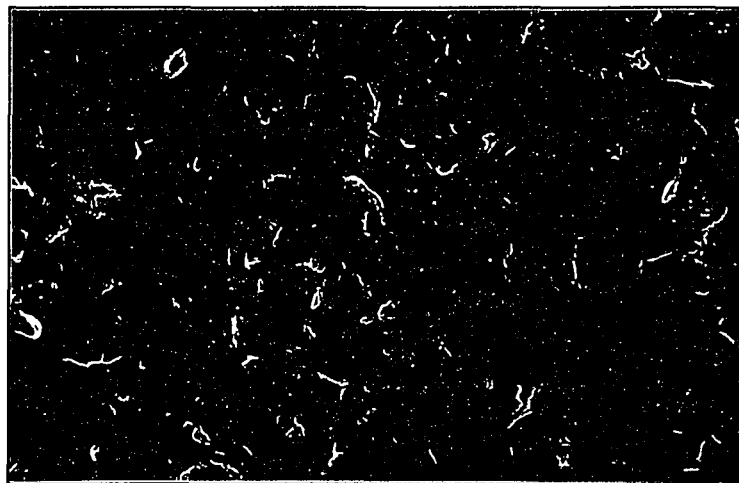
100 μm

Figure 5.3: Micrograph of sample # 1 substrate roughened by sandblasting.



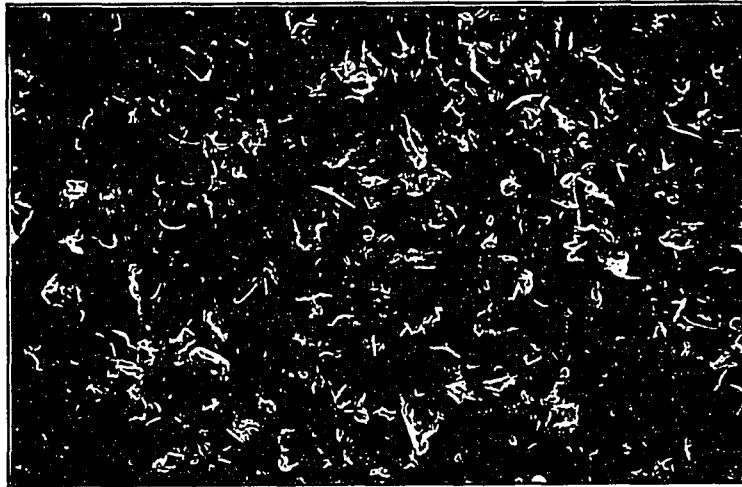
↔
100 μm

Figure 5.4: Micrograph of sample # 2 substrate roughened by sandblasting.



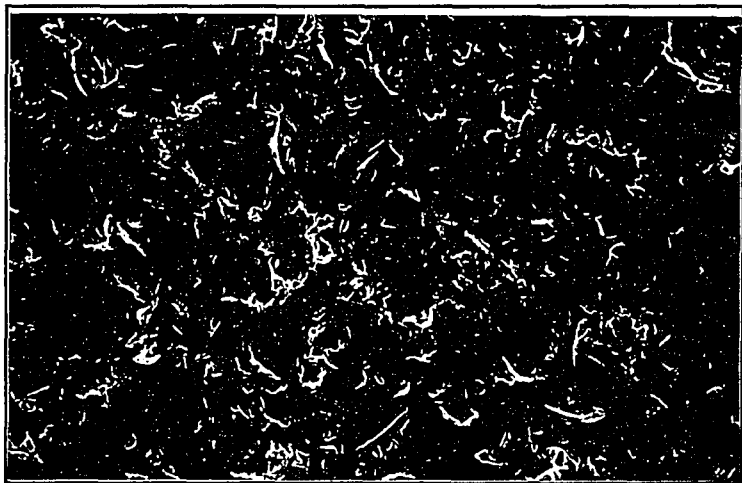
↔
100 μm

Figure 5.5: Micrograph of sample # 3 substrate roughened by sandblasting.



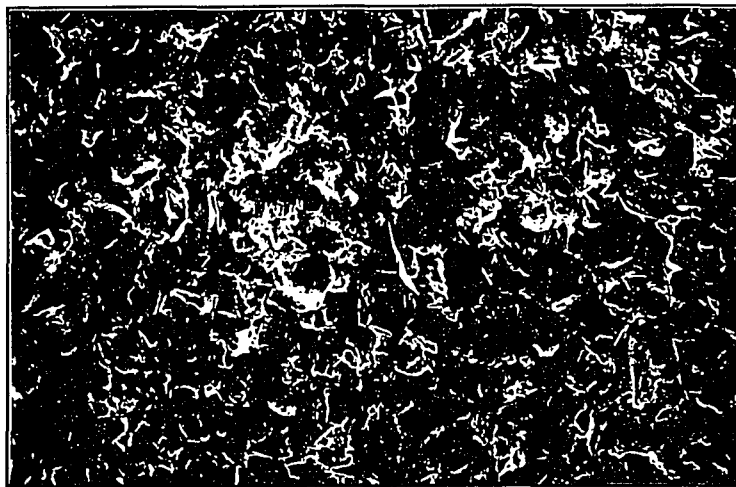
↔
100 μm

Figure 5.6: Micrograph of sample # 4 substrate roughened by sandblasting.



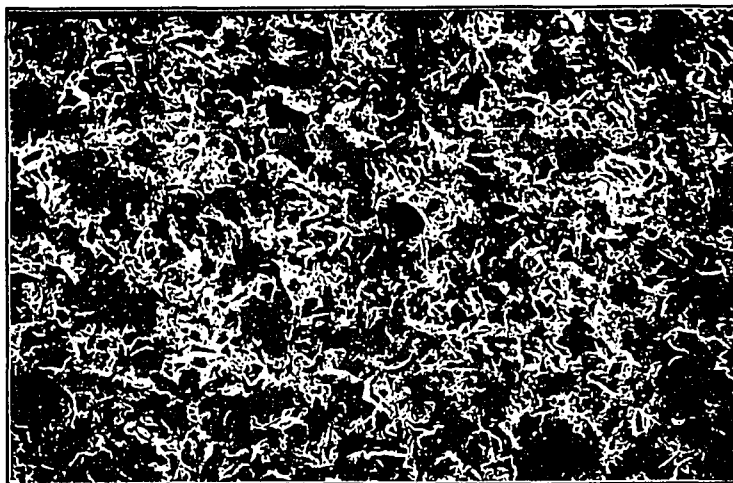
↔
100 μm

Figure 5.7: Micrograph of sample # 5 substrate roughened by sandblasting.



↔
100 μm

Figure 5.8: Micrograph of sample # 6 substrate roughened by sandblasting.



↔
100 μm

Figure 5.9: Micrograph of sample # 7 substrate roughened by sandblasting.

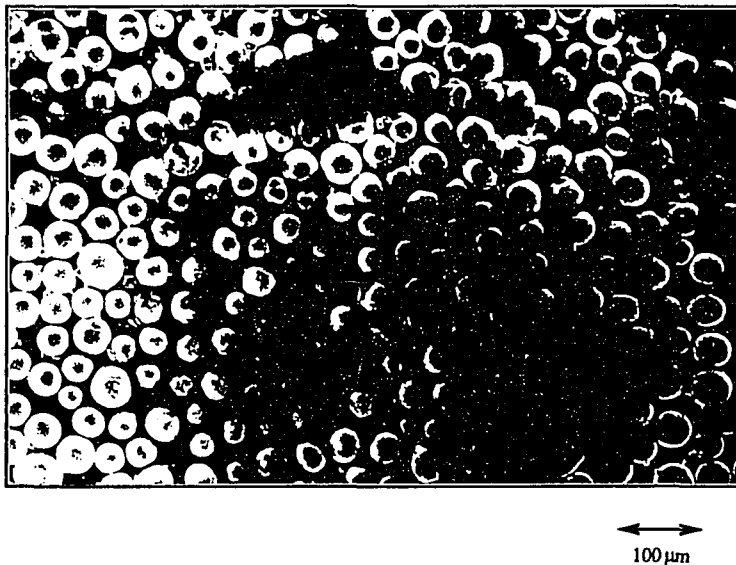
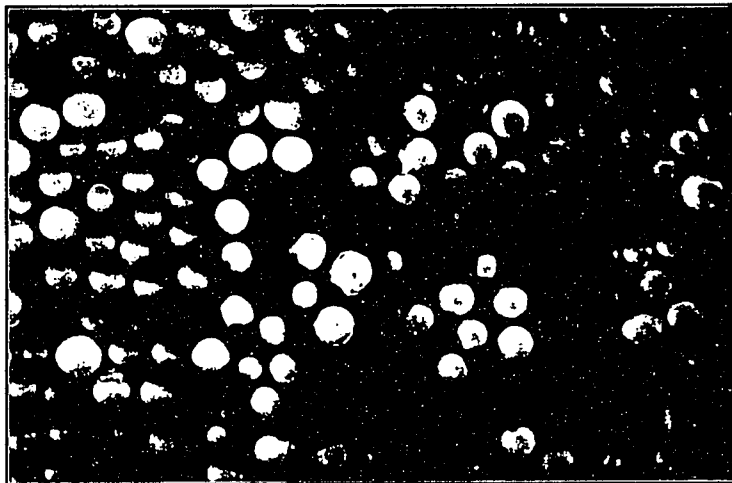


Figure 5.10: Micrograph of diffuse surface sample # 10.

Another two samples # 10 and # 11 were commercial diffuse surfaces. These surfaces were made of glass spheres. The sizes of glass sphere range from $30 \mu m$ to $50 \mu m$. The distance between neighboring glass spheres varies roughly from $0 \mu m$ to $30 \mu m$. See Figure 5.10 and Figure 5.11 for surface structure detail. These surfaces were used to study the change of the index of refraction. A micrograph of sample # 10 is shown in Figure 5.10. Sample # 11 was identical to sample # 10 but it was coated with a layer of 500\AA thick aluminum. The aluminum was deposited by vacuum deposition under 10^{-6} torr high vacuum. This coating changed the index of refraction but did not change the surface profile. The micrograph of the sample # 11 is shown in Figure 5.11.



↔
100 μm

Figure 5.11: Micrograph of aluminum coated diffuse surface sample # 11.

CHAPTER 6

THE MEASUREMENTS

Light scattering from perfect smooth surfaces, perturbed (slightly rough) surfaces, and very rough surfaces have been studied by using the nephelometer to measure the Mueller matrix elements. The Mueller matrix elements S_{ij} are a signature of surface quality and the S_{ij} must respond to surface changes. The samples were placed in some orientation α at the scattering position. The reflection, scattering, and absorption depended on the surface structure and optical constants. At the same time, the detector measured the intensity and polarization of the scattered light as a function of scattering angle θ . This θ -dependent signal obtained from the combination of input-output optical devices was a particular matrix element S_{ij} for a particular surface orientation α . Therefore a complete signature consists of all 16 matrix element curves which contain all the scattering information available at $441.6nm$ (He-Cd Laser).

All the 16 Mueller matrix elements were measured for the case of near grazing incident angle ($\alpha \approx 15^\circ$) ($\approx 75^\circ$ from normal) for the sample # 4. Measurements shown in Figure 6.1, are representative of the entire 16 Mueller matrix elements of a surface. The four unique matrix elements S_{11} , S_{12} , S_{33} , and S_{34} were also measured as function of incident angle α for all eight aluminum substrate. The specific angles of incidence α were equal

to 15° , 30° , 45° , 60° , and 75° (75° , 60° , 45° , 30° , and 15° from the normal respectively). These results are shown from Figure 6.2 to Figure 6.9.

The samples # 10 and # 11 were used to study the effects of the change of reflective index. All the 16 Mueller matrix elements were measured for the case of 45° , and 90° (45° and 0° from normal) before and after the aluminum coating. These data are shown from Figure 6.10 to Figure 6.13.

Because of the total intensity of light scattered from these samples changes drastically with angle, the logarithms are taken before the first column elements are plotted. The other twelve elements were measured in the polarization mode. The signals from a scatterer will vary between -100% and $+100\%$ indicating the efficiency for converting the input Stokes vector component to the output Stokes vector component. All the polarization matrix elements were plotted in percentage vs. scattering angles. We therefore get the polarization conversion efficiency for this scatterer.

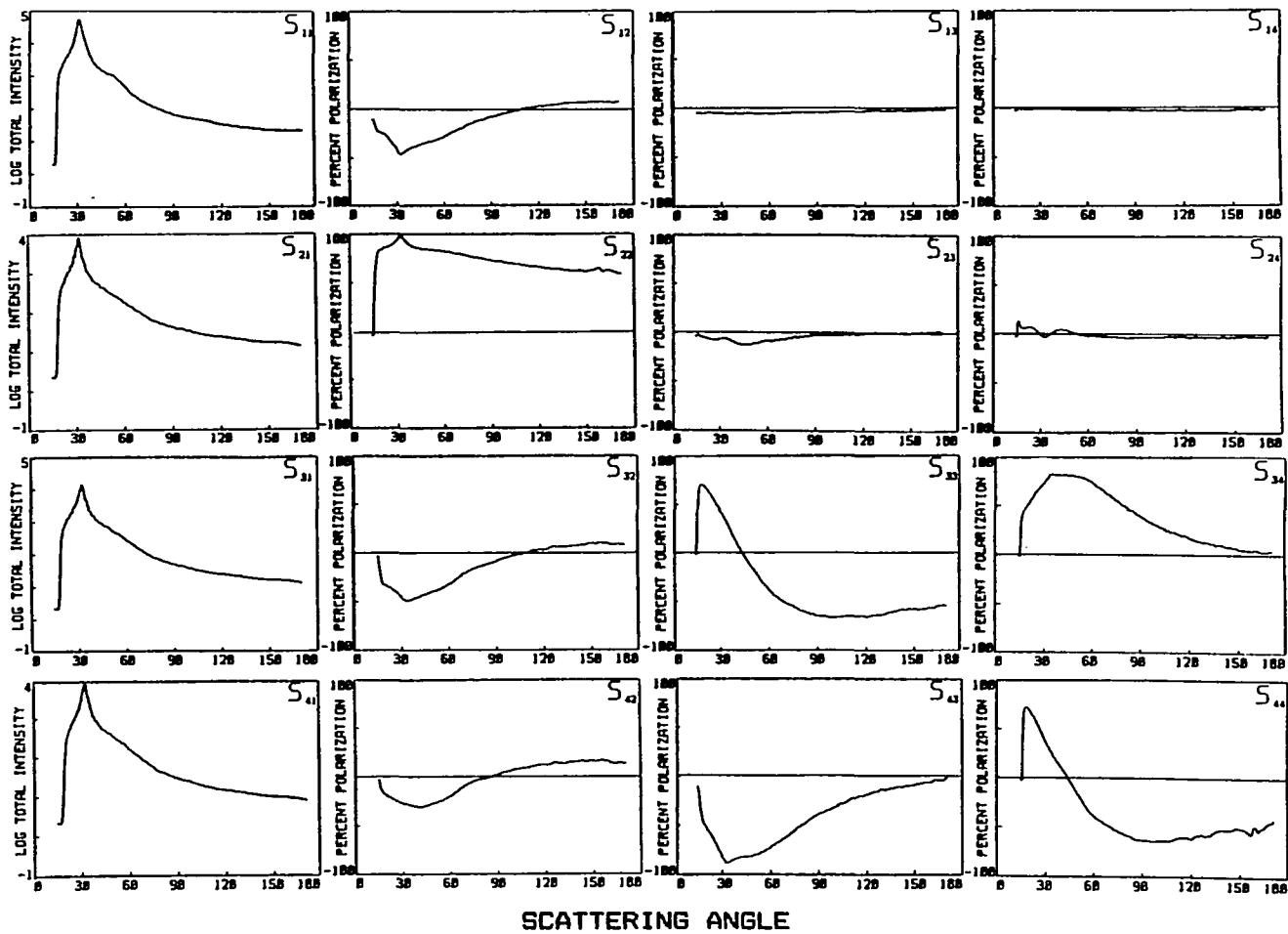


Figure 6.1: Experimental measurements of the sixteen light scattering Mueller matrix elements of a substrate # 4 (slightly roughened) illuminated at grazing incident angle $\alpha \approx 15^\circ$ ($\lambda = 441.6nm$).

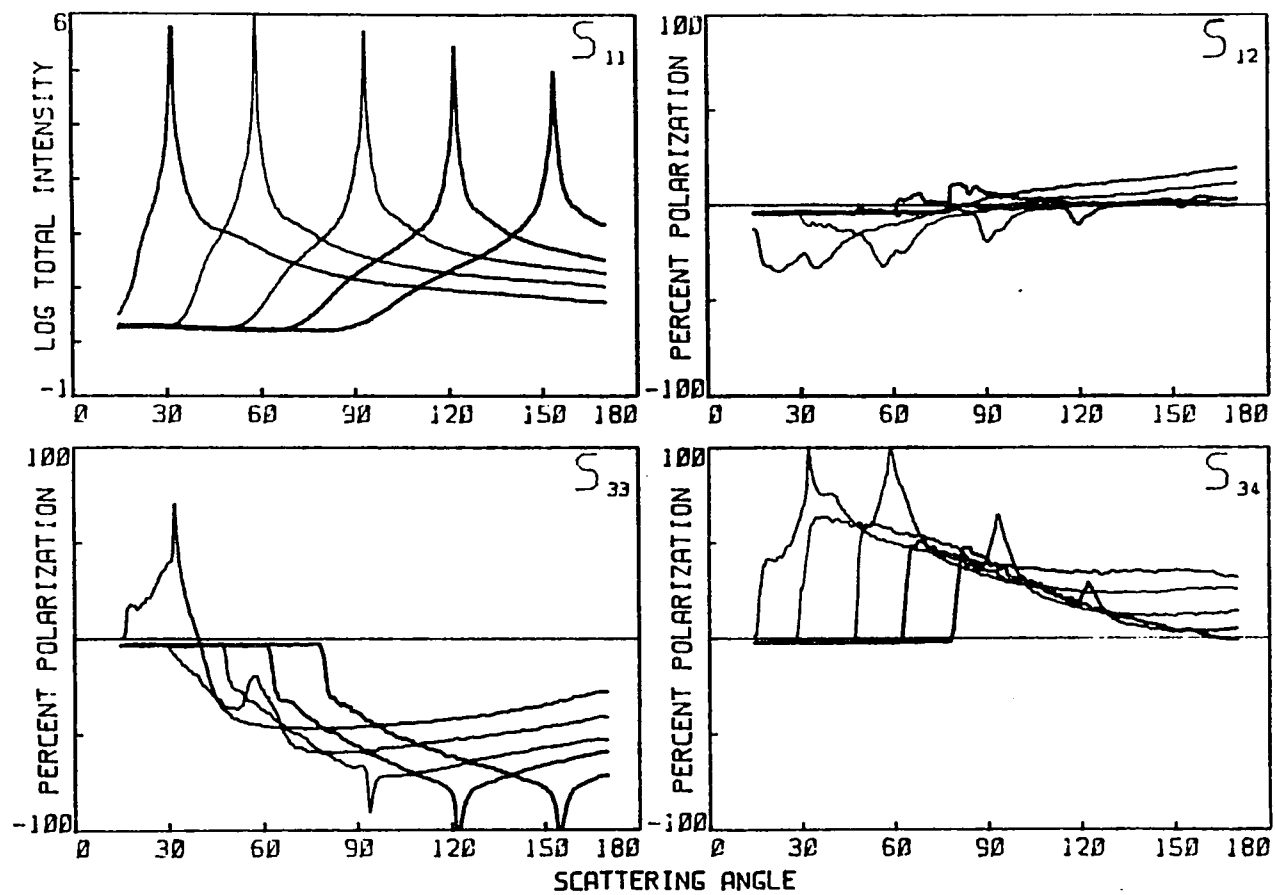


Figure 6.2: Experimental measurements of the four light scattering Mueller matrix elements of a substrate # 0 illuminated at $\alpha = 15^\circ, 30^\circ, 45^\circ, 60^\circ,$ and 75° ($\lambda = 441.6nm$).

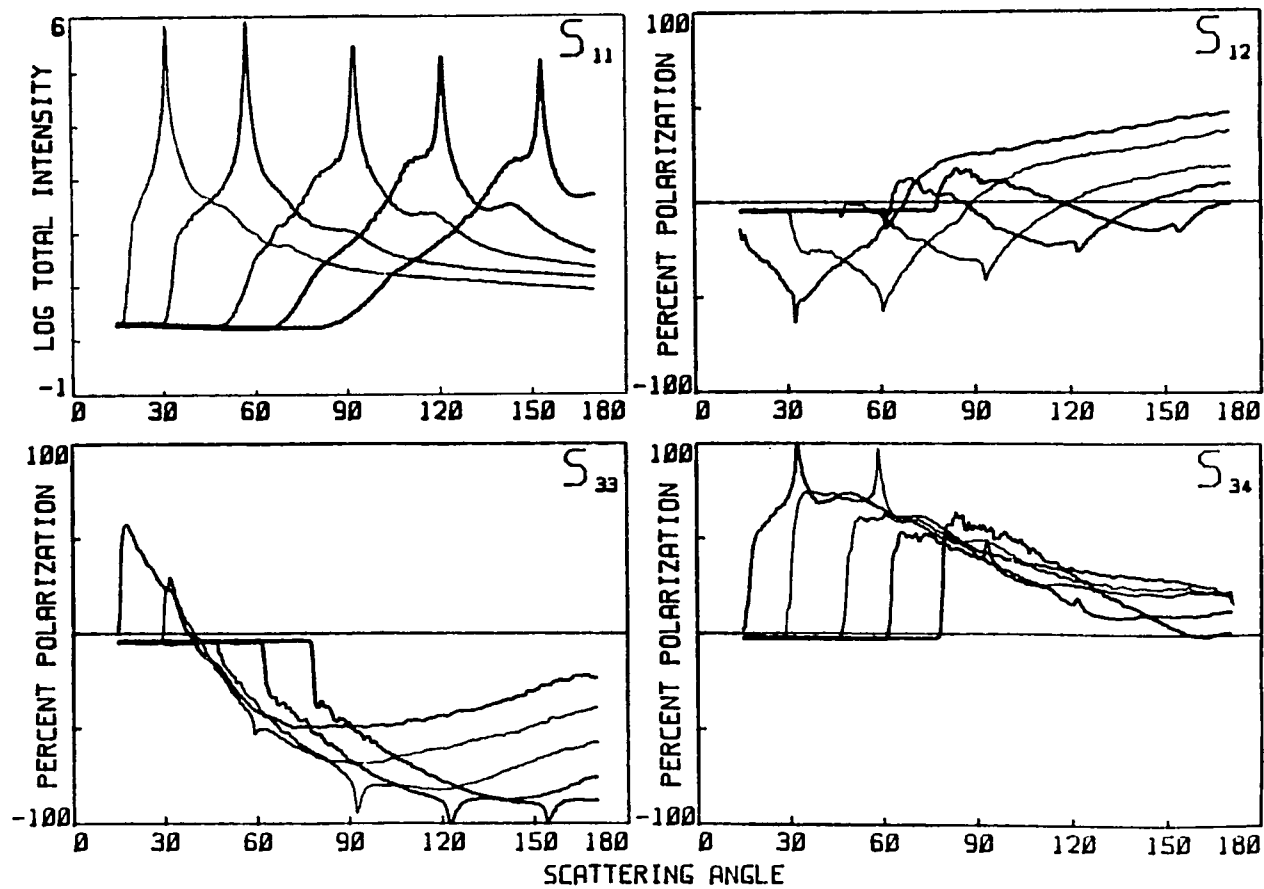


Figure 6.3: Experimental measurements of the four light scattering Mueller matrix elements of a substrate # 1 illuminated at $\alpha = 15^\circ, 30^\circ, 45^\circ, 60^\circ,$ and 75° ($\lambda = 441.6nm$).

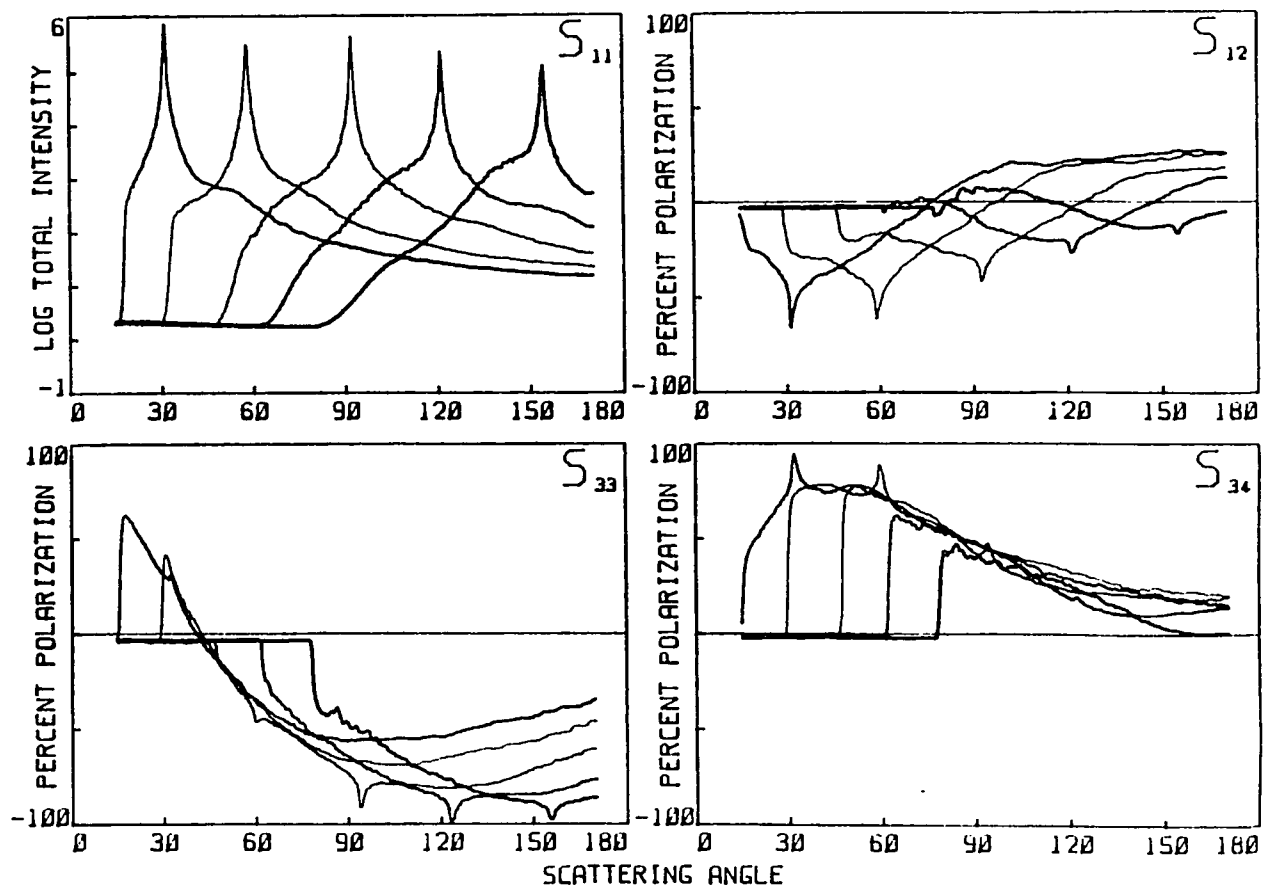


Figure 6.4: Experimental measurements of the four light scattering Mueller matrix elements of a substrate # 2 illuminated at $\alpha = 15^\circ, 30^\circ, 45^\circ, 60^\circ,$ and 75° ($\lambda = 441.6nm$).

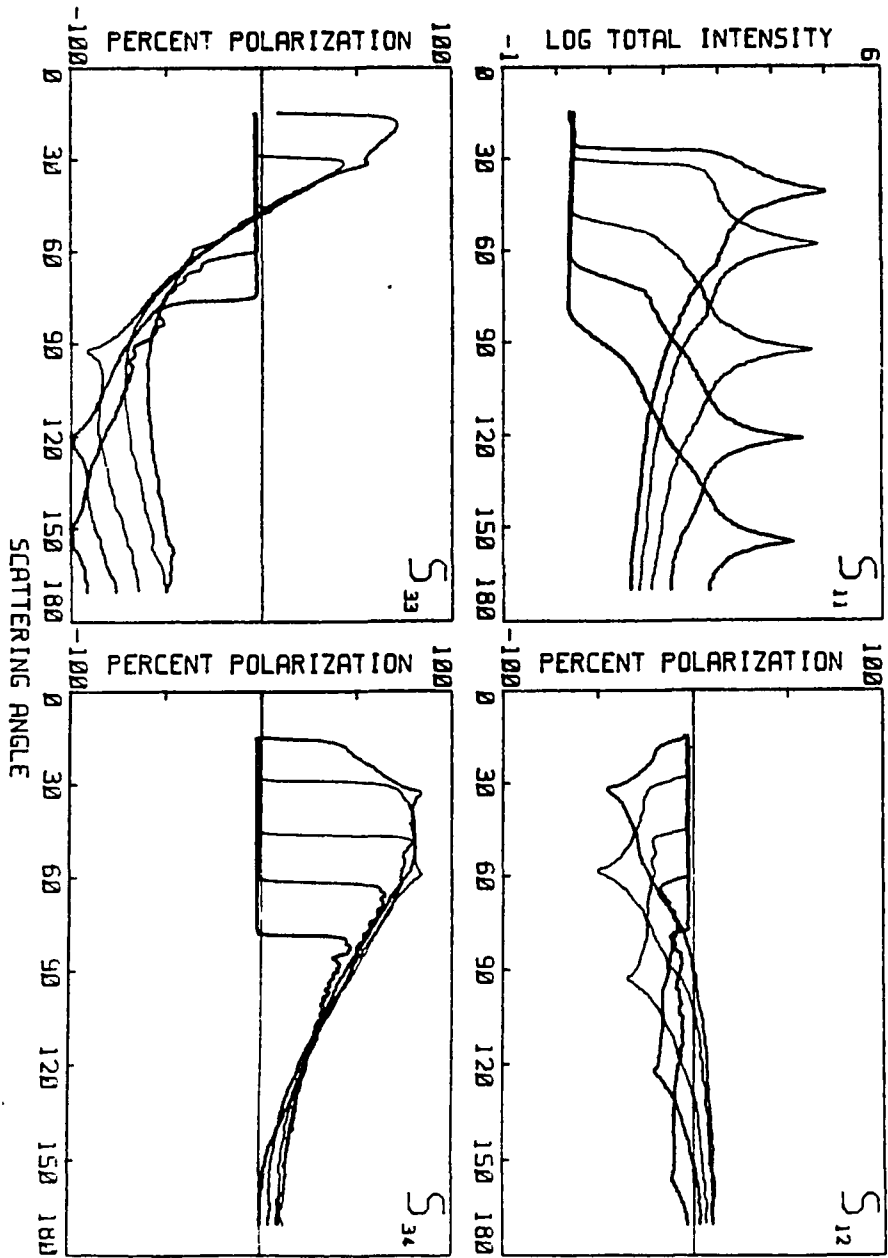


Figure 6.5: Experimental measurements of the four light scattering Mueller matrix elements of a substrate # 3 illuminated at $\alpha = 15^\circ, 30^\circ, 45^\circ, 60^\circ$, and 75° ($\lambda = 441.6nm$).

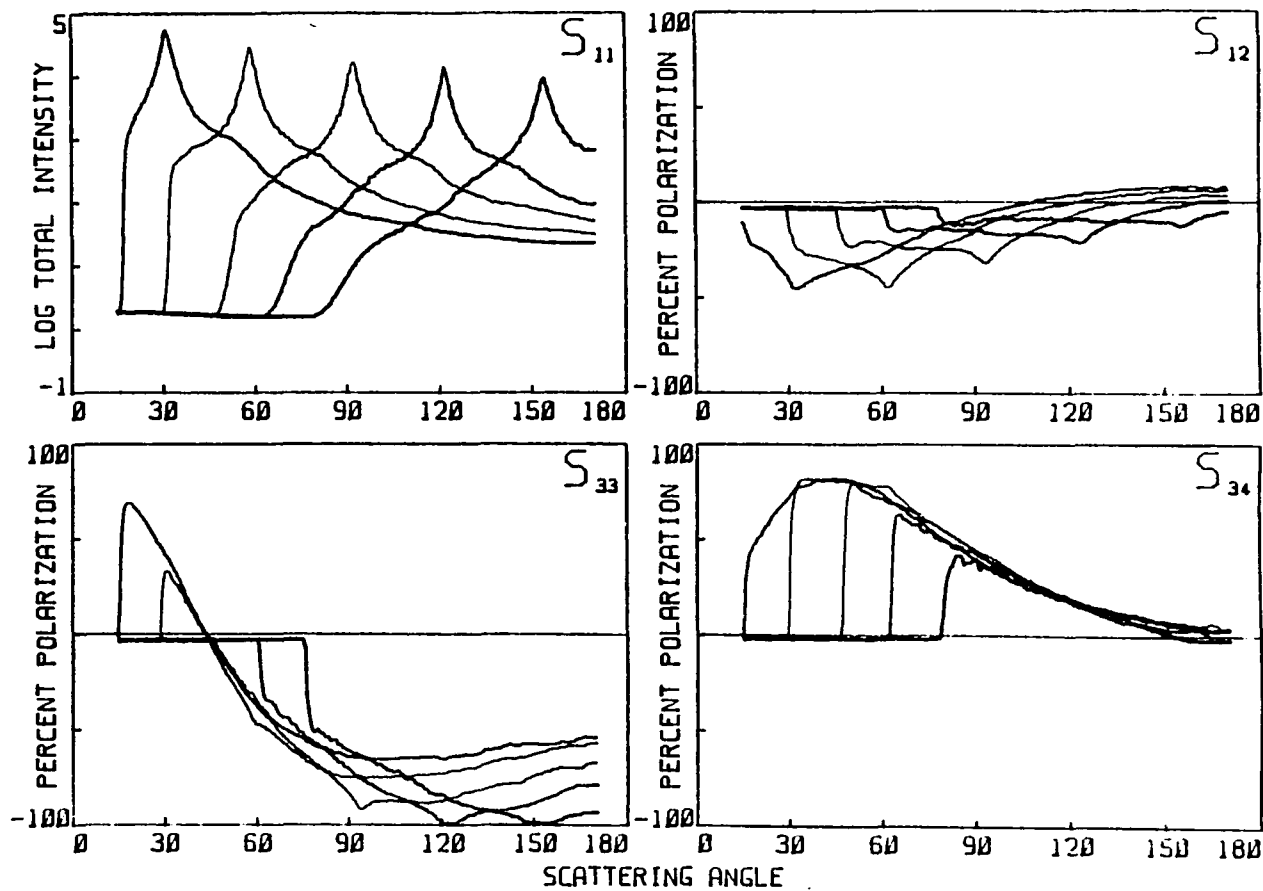


Figure 6.6: Experimental measurements of the four light scattering Mueller matrix elements of a substrate # 4 illuminated at $\alpha = 15^\circ, 30^\circ, 45^\circ, 60^\circ,$ and 75° ($\lambda = 441.6nm$).

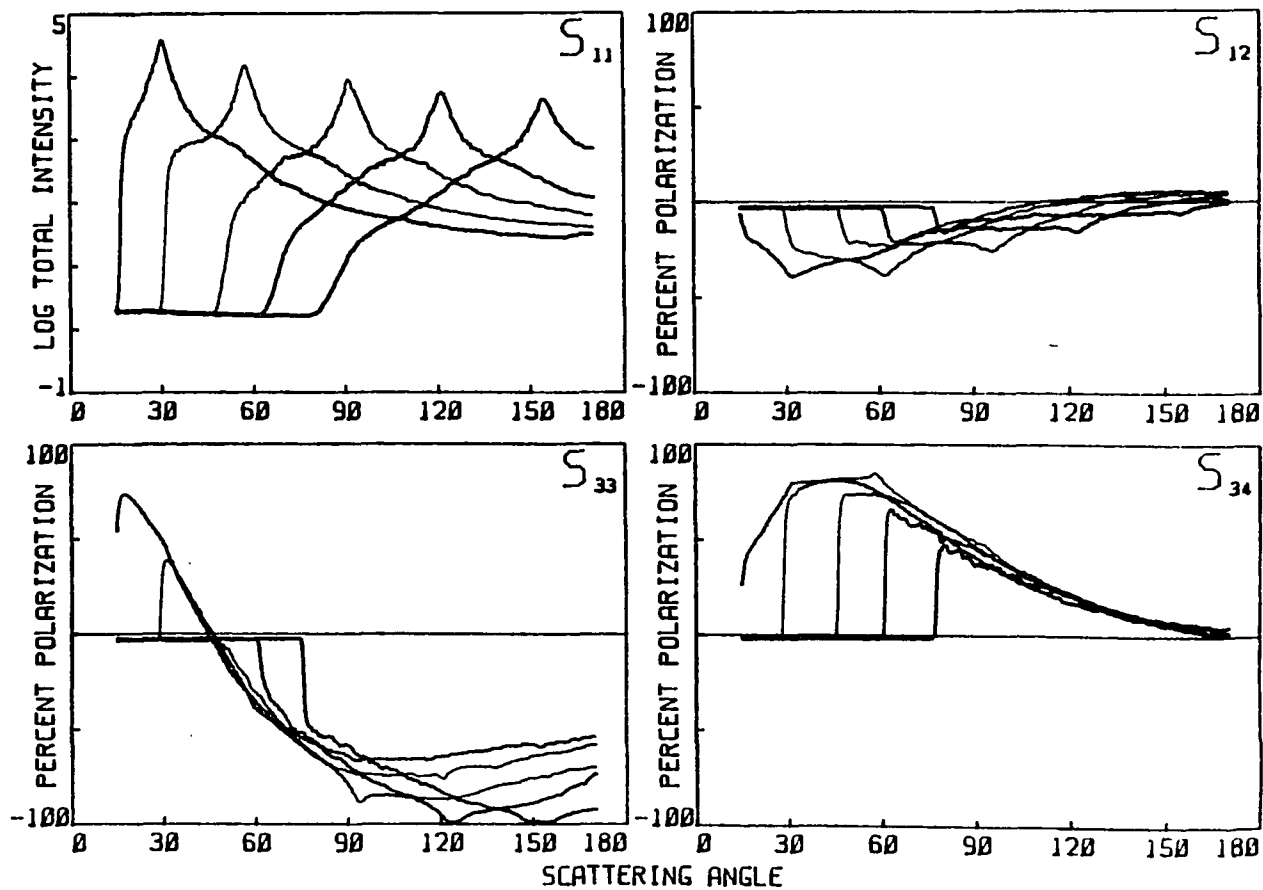


Figure 6.7: Experimental measurements of the four light scattering Mueller matrix elements of a substrate # 5 illuminated at $\alpha = 15^\circ, 30^\circ, 45^\circ, 60^\circ,$ and 75° ($\lambda = 441.6nm$).

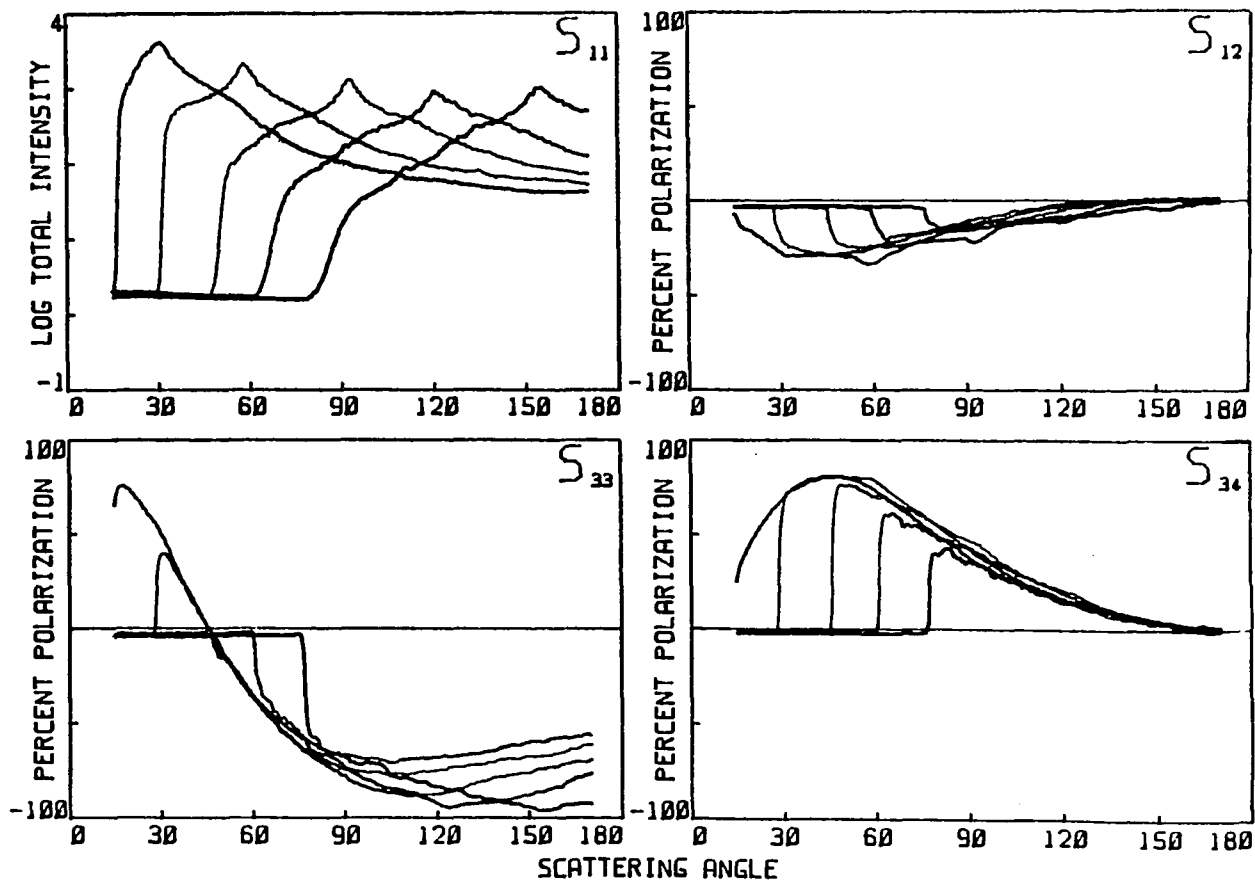


Figure 6.8: Experimental measurements of the four light scattering Mueller matrix elements of a substrate # 6 illuminated at $\alpha = 15^\circ, 30^\circ, 45^\circ, 60^\circ,$ and 75° ($\lambda = 441.6nm$).

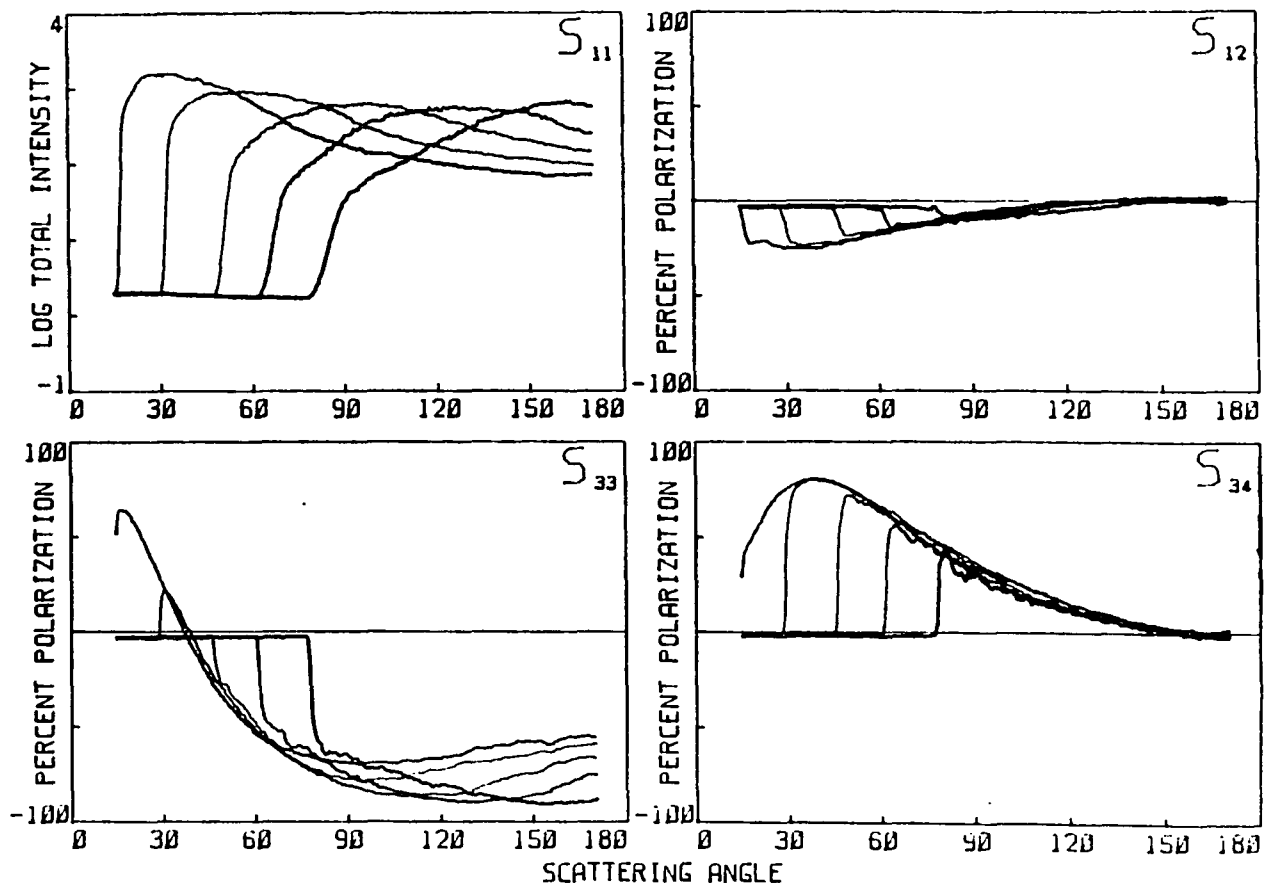


Figure 6.9: Experimental measurements of the four light scattering Mueller matrix elements of a substrate # 7 illuminated at $\alpha = 15^\circ, 30^\circ, 45^\circ, 60^\circ,$ and 75° ($\lambda = 441.6nm$).

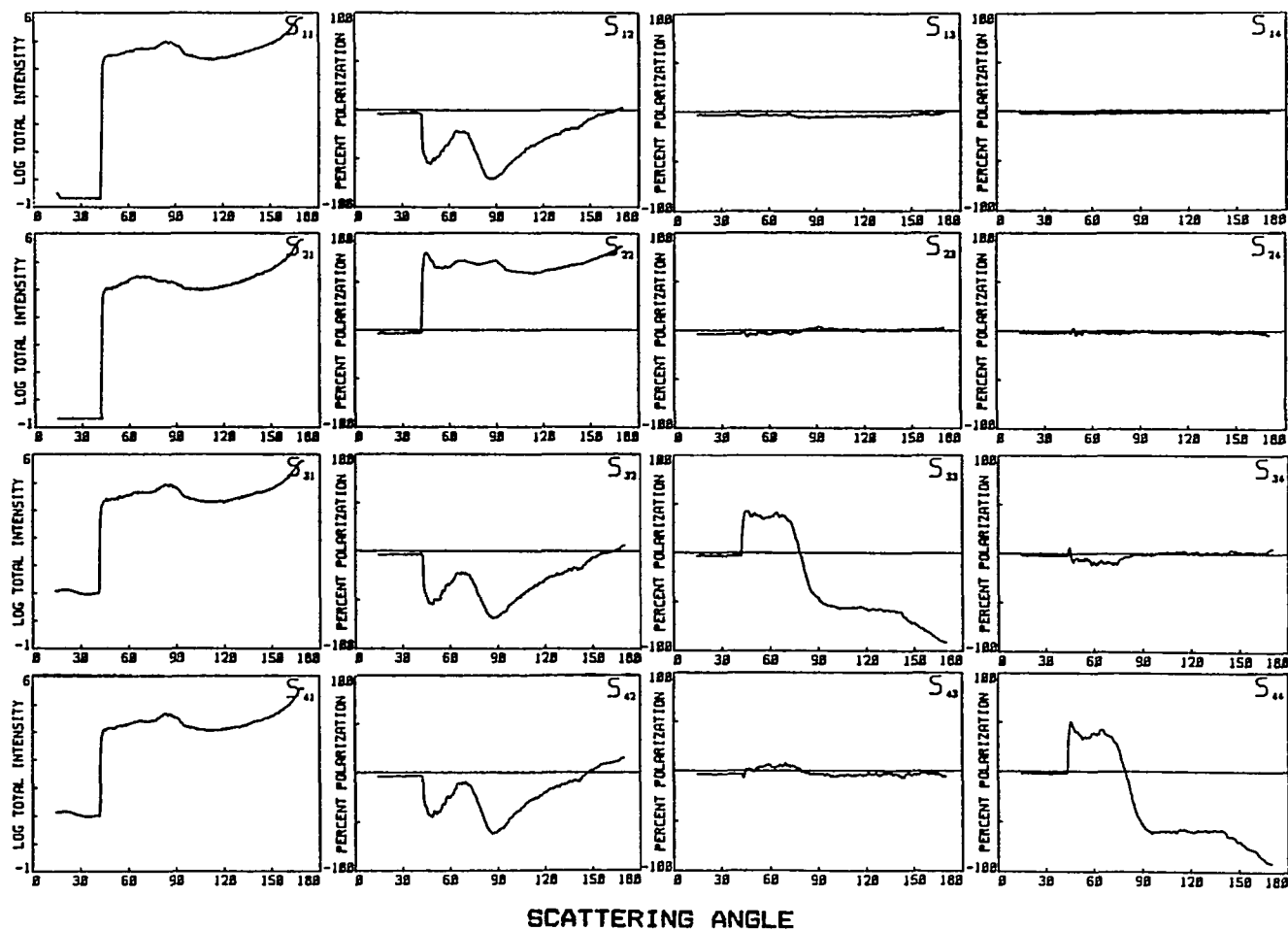


Figure 6.10: Experimental measurements of the sixteen light scattering Mueller matrix elements of a diffuse surface # 10 (before aluminum coating) illuminated at $\alpha = 45^\circ$.

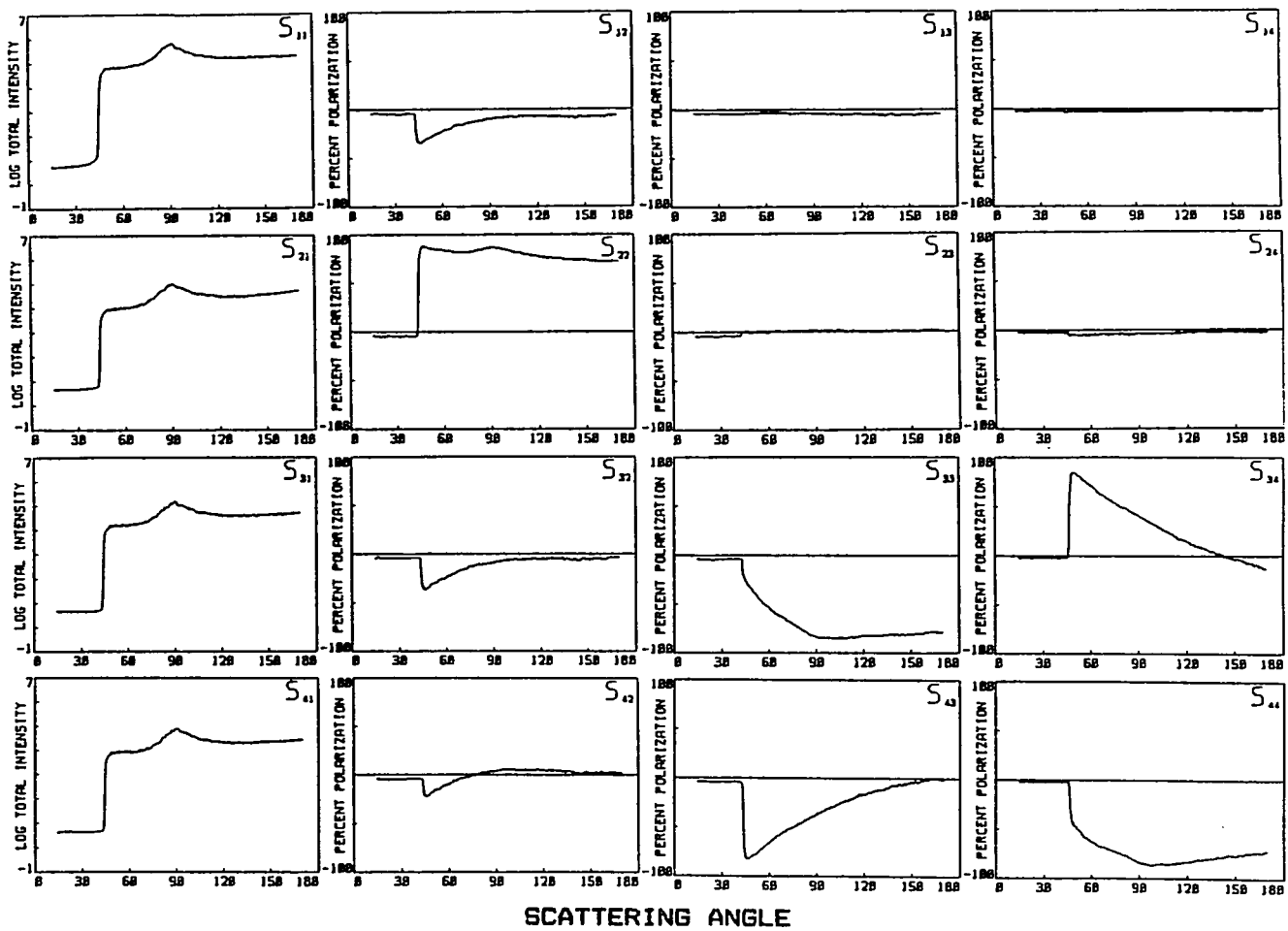


Figure 6.11: Experimental measurements of the sixteen light scattering Mueller matrix elements of an aluminum coated diffuse surface # 11 illuminated at $\alpha = 45^\circ$.

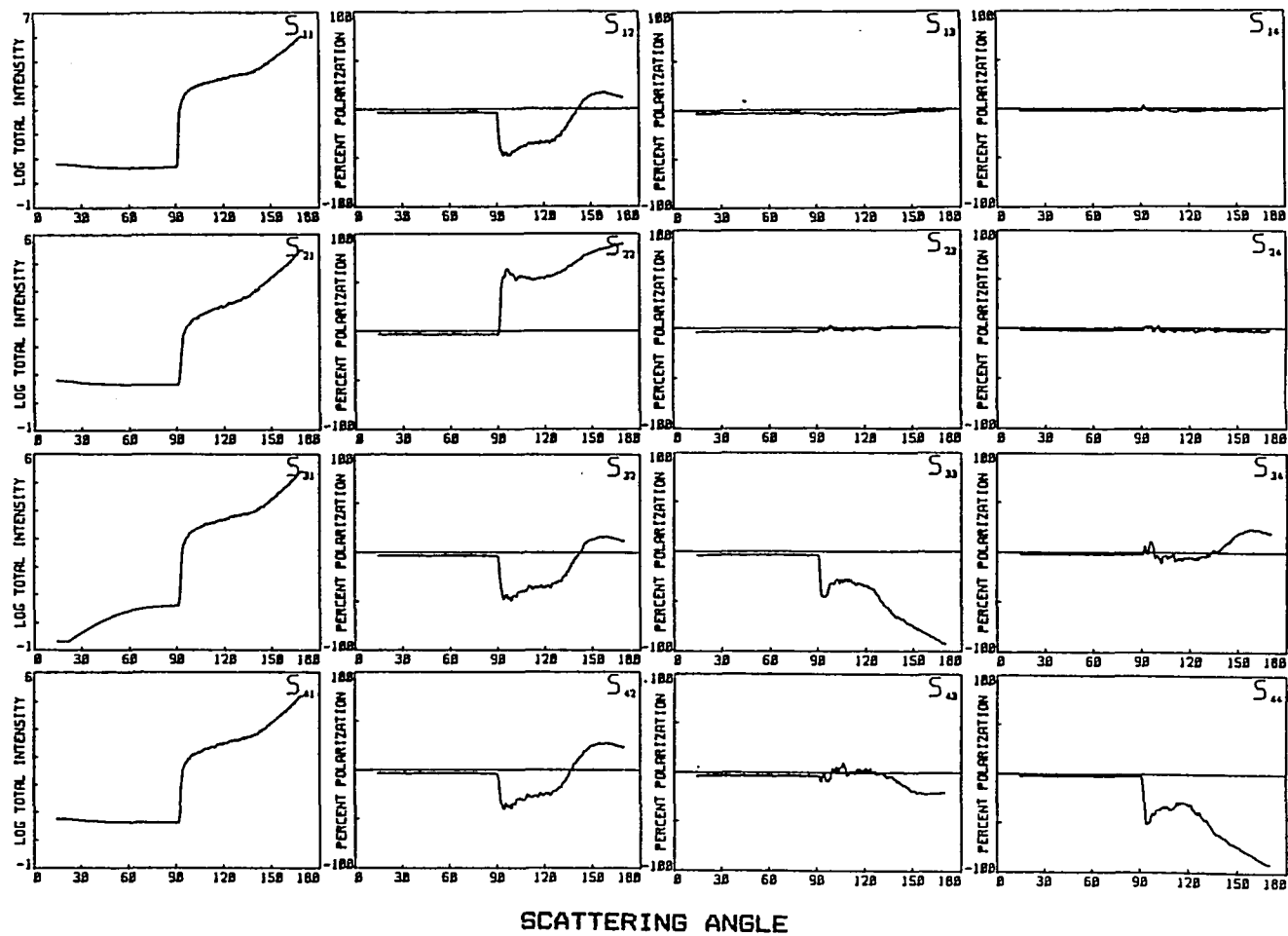


Figure 6.12: Experimental measurements of the sixteen light scattering Mueller matrix elements of a diffuse surface # 10 (before aluminum coating) illuminated at $\alpha = 90^\circ$.

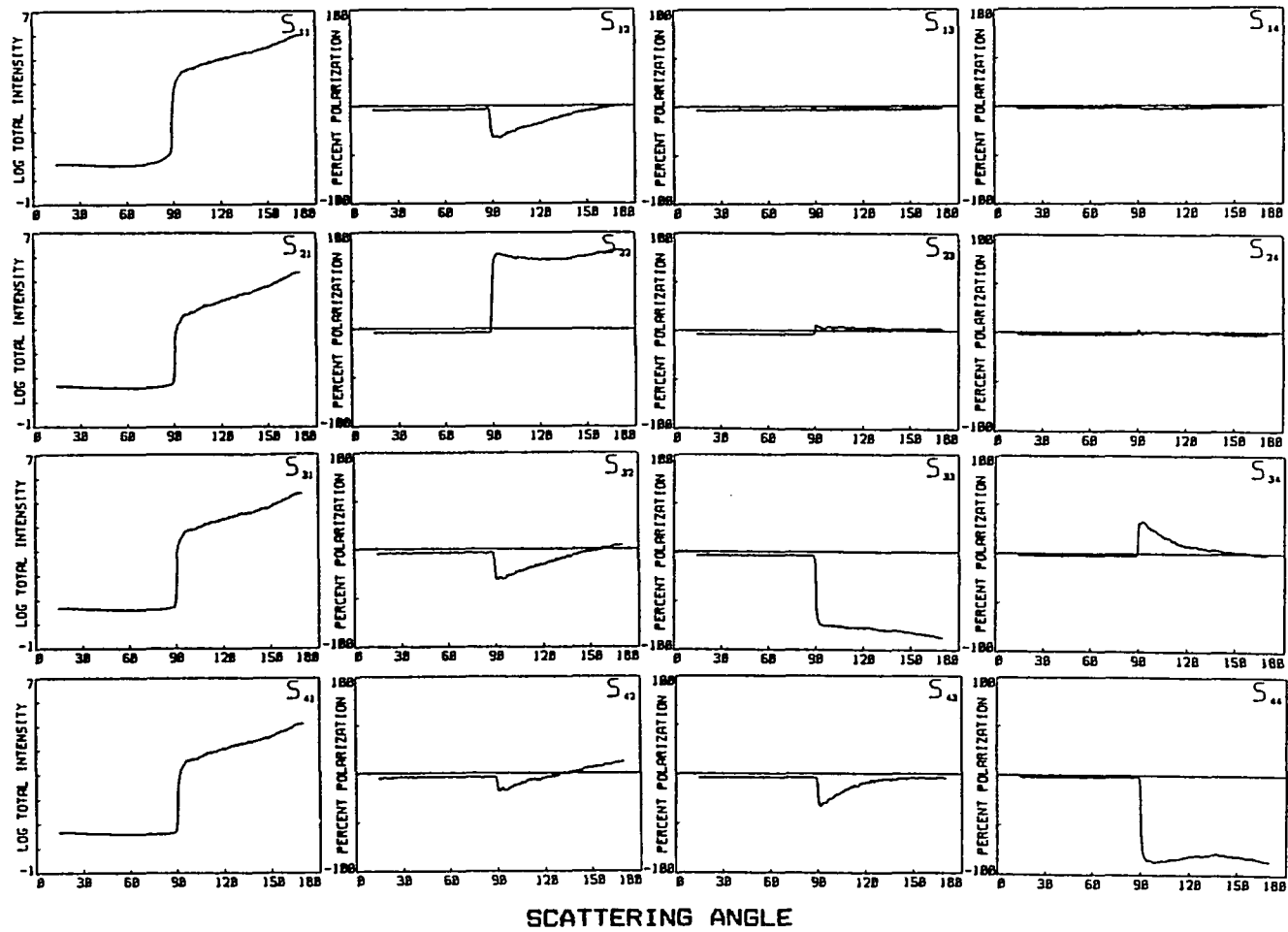


Figure 6.13: Experimental measurements of the sixteen light scattering Mueller matrix elements of an aluminum coated diffuse surface # 11 illuminated at $\alpha = 90^\circ$.

CHAPTER 7

RESULTS

All the 16 Mueller matrix elements were investigated for the rough surface # 4 and plotted in Figure 6.1. These curves give all the information for the surface and show that only 4 unique matrix elements (S_{11} , S_{12} , S_{33} , and S_{34}) need to be measured. Iafelice [9] mentioned that for a sufficiently symmetric scattering system, some elements are zero ($S_{13} = S_{14} = S_{23} = S_{24} = 0$), some are identical ($S_{12} = S_{32} = S_{42}$; $S_{11} = S_{31} = S_{41}$), some are inverse ($S_{34} = -S_{43}$), and some are combinations of matrix elements ($S_{21} = S_{11} + S_{12}$ but $S_{11} = S_{22}$ for the spherical particle). These results are also shown in Figure 6.1.

7.1 Mueller Matrix Elements for Rough Surface

The 4 unique matrix elements were measured as a function of the illumination angle α from grazing to near normal incidence (when sample is illuminated at angle α , the $\theta_{scat} = \alpha$ to 180° . See Figure 4.1 for detail.) for all aluminum samples. This study was performed to see how sensitive the matrix elements are to the different illumination angles and surface variation.

Consider the total intensity S_{11} . We get higher intensity for smaller incident angles α and lower intensity for larger incident angles at specular peak. This phenomenon is not

so prominent when the surface is very rough. This shows in Figure 6.9. On the contrary, smaller incident angles have lower scattering intensity and larger incident angles have higher scattering intensity. This phenomenon is still very prominent when surface is very rough. Surface roughness also can be distinguished by S_{11} . Smoother surfaces have higher intensity and rougher surfaces have lower intensity. This is true for both the specular peak and the scattered light.

For the S_{12} , except for sample # 0, it shows that smaller incident angles have lower percent polarization at the specular peak and higher percent polarization in the scattering region. On the other hand, larger incident angles have higher percent polarization at the specular peak and lower percent polarization in the scattering region. These phenomena will be wiped out with the increasing surface roughness. The S_{12} in Figure 6.9 for sample # 7 are similar for different incident angles whereas the percent polarization becomes smaller with the surface roughness. The polarization approaches zero when the surface roughness becomes saturated (adding more defects to the surface does not affect the scattering). This phenomenon represents the well known masking curve[14]. These properties are not true for the smoothest surface sample # 0.

The S_{33} is strongly dependent on incident angles. For the conducting surface, the curves start from positive percent polarization and go to negative percent polarization for 15° and 30° incident angles only. The other incident angles start with negative polarization for all the θ scans. The incident angles smaller than 40° have a positive percent polarization but have a negative percent polarization for angles larger than 40°. This is true for all aluminum samples except sample # 0 in this study. For the non-conducting

surface, the polarization will not have this property (see Figure 6.10). But S_{33} still goes to negative percent polarization in the backscattering region (see Figure 6.10 to Figure 6.13). In the backscattering region, we can see that both smooth surfaces and rough surfaces are sensitive to a change in the incident angle. S_{33} shows that smaller incident angles have higher percent scattering polarization and larger incident angles have lower percent scattering polarization in the backscattering region. At the same time, the surface roughness information could be decided at the negative percent polarization area (after 40°). The smoother surfaces have sharp negative polarization specular peaks. For the rougher surfaces, the negative polarization specular peaks are not so sharp. No specular peaks are seen at all in the roughest surface sample # 7 (see Figure 6.9). Unfortunately, surface roughness is independent of the percent polarization in the backscattering region, therefore; surface roughness information can't be obtained at backscattering angles.

For the S_{34} , the polarization for different incident angles is more sensitive to the surface roughness. The percent polarization decreases with increasing the incident angles for smoothest surface only at the specular peak and in the backscattering region. On the other hand, the percent polarization for S_{34} is independent of illumination angles for rougher surface. The polarization gradually loses its phase information with increasing surface roughness. When the surface becomes very rough, different illumination angles give the same percent polarization. S_{34} for the roughest surface sample # 7 has the same percent polarization for different incident angles (see Figure 6.9 for this phenomenon).

7.2 Change Index of Reflection for Rough Surface

The complete 16 Mueller matrix elements for study the change of refractive index are given in Figure 6.10 to Figure 6.13. Only five matrix elements S_{11} , S_{12} , S_{22} , S_{33} , and S_{34} are independent after comparing with all the 16 matrix elements measurements for the diffuse surfaces sample # 10 and sample # 11. Figure 6.10 and Figure 6.11 show the Mueller matrix elements illuminated at 45° for non-conducting (non-absorbing) and conducting (absorbing) diffuse surface respectively. Figure 6.12 and Figure 6.13 represent the Mueller matrix elements illuminated at 90° for non-conduction and conduction diffuse surface respectively.

7.2.1 45° Incidence

For the S_{11} , the backscattering intensity from the non-absorbing diffuse surface (uncoated with aluminum) is stronger than the intensity from the absorbing diffuse surface (aluminum coated). At other scattering angles, the scattering intensity from the absorbing diffuse surface is higher than from the non-absorbing diffuse surface.

For the S_{12} , the polarization fluctuates in the scattering region before 90° after which the percent polarization increases and approaches zero for the non-absorbing (uncoated) diffuse surface. On the other hand, the polarization increases and approaches zero without any distinguishable fluctuations for the absorbing (aluminum coated) diffuse surface. The percent scattering polarization for the coated surface is higher than those for the uncoated surface.

For the S_{22} , the percent polarization for a non-absorbing diffuse surface is about 5% to 10% lower than absorbing diffuse surface at scattering angles before 150° . At the backscattering angles (about after 150°), the percent polarization from non-absorbing diffuse surface is higher than for the absorbing diffuse surface.

For the S_{33} , the percent polarization before 80° is positive. After 80° the percent polarization decreases for the uncoated diffuse surface. The percent polarization for the coated diffuse surface starts decreasing at 45° and reaches its minimum at 90° .

For the S_{34} , the percent polarization for uncoated diffuse rough surfaces is almost zero for all scattering angles. On the contrary, the percent polarization is at its maximum at 45° and then decreases to zero for the aluminum coated diffuse surface.

7.2.2 90° Incidence

The Mueller matrix elements for uncoated and coated diffuse rough surfaces illuminated at 90° incidence are not drastically different than those illuminated at 45° . S_{11} for uncoated and coated diffuse surface are similar but the intensity for the uncoated surface is about one order of magnitude lower. For S_{12} , the percent polarization for the uncoated diffuse surface is 10% lower than the polarization of coated surface and it reaches a positive polarization and then approaches zero. For S_{22} , the percent polarization from the uncoated diffuse surface is from 20% to few percent lower than those of coated diffuse surface. The percent polarization is the same for scattering angles greater than 140° . For S_{33} , the percent polarization for the aluminum coated diffuse surface is much lower (it varies from 75% to a few percent) than for the uncoated diffuse surface. For S_{34} ,

again the percent polarization fluctuates around 0% for the uncoated diffuse surface. For the coated diffuse surface, the polarization starts around 10% then approaches zero as scattering angle increases.

7.3 Conclusion

7.3.1 Sandblasted Aluminum Rough Surface

In the study of light scattering as a function of incident angle for a rough surface, the S_{ij} strongly depend on the incident angle α .

Although S_{11} depends on the incident angles and surface roughness at its specular peak, S_{11} strongly depends on the incident angles and surface roughness in the backscattering region. In the backscattering region, the scattering information does not change with either change the incident angle or surface roughness. Therefore, the backscattering signal for S_{11} can be used to determine the incident angle or to study the degree of surface roughness.

S_{12} is still dependent on the incident angle and surface roughness both at the specular peak and in the backscattering region for smoother surfaces. As the surface becomes rougher, S_{12} is not sensitive to the change of incident angle or surface variations. This phenomenon is related to the masking effect - where certain surface features become invisible and undetectable.

For S_{33} , the percent polarizations are positive before 40° and negative after 40° . This phenomenon shows that 40° (approximately) is a critical point for S_{33} . Positive polarization (before 40°) can be used to distinguish the incident angle smaller than 40° for

conducting surface. In the backscattering region, S_{33} is sensitive to a change in the incident angle. The change of incident angle can be distinguished by the degree of polarization easily. Surface roughness information can be distinguished by S_{33} from the negative specular peak polarization but not from the percent polarization in the backscattering area.

For smoother surfaces, S_{34} is dependent on incident angle and surface variation at the specular peak angle. S_{34} is independent of illumination angle and surface geometry at all scattering angles. Figure 6.9 shows this example.

A summary of the distinguishing ability for illumination angles and surface variations for the four Mueller matrix elements is shown in Table 7.1.

7.3.2 Diffuse Surface

Our study of light scattering by changing index of reflection and the angle of incidence α , show that the efficiency of converting polarization for the case of 45° incident angle is higher compared with the case for 90° either before or after the surface coating. Another interesting phenomenon is that the S_{34} polarization changes from zero to positive polarization. This is because the index of refraction for a non-absorbing medium is real, so the polarization for S_{34} is zero, while the index of refraction for absorbing medium is complex, so the polarization for S_{34} is nonzero. This was verified experimentally. Therefore, S_{34} is the best Mueller matrix element for distinguishing the non-absorbing and absorbing media. Table 7.2 shows the distinguishing ability of the Mueller matrix elements for non-absorbing and absorbing diffuse surfaces.

S_{11}		
<i>position</i>	<i>illumination angles α</i>	<i>surface roughness σ</i>
<i>specular peak</i>	intensity decreases with increasing incident angle	intensity decreases with increasing surface roughness
<i>backscattering region</i>	intensity increases with increasing incident angles	intensity decreases with increasing surface roughness
specular peak and backscattering region can be used to distinguish illumination angle and surface variation		
S_{12} (except sample # 0)		
<i>position</i>	<i>illumination angles α</i>	<i>surface roughness σ</i>
<i>specular peak</i>	polarization increases with increasing incident angle	polarization increases with increasing surface roughness
<i>backscattering region</i>	polarization decreases with increasing incident angles	polarization decreases with increasing surface roughness
specular peak and backscattering region can be used to distinguish illumination angle and surface variation for smoother surface only		
S_{33} (except sample # 0)		
<i>position</i>	<i>illumination angles α</i>	<i>surface roughness σ</i>
<i>specular peak</i>	polarization decreases with increasing incident angle	distinguish ability is not prominent
<i>backscattering region</i>	polarization decreases with increasing incident angles	distinguish ability is not prominent
specular peak and backscattering region can be used to distinguish illumination angle		
S_{34}		
<i>position</i>	<i>illumination angles α</i>	<i>surface roughness σ</i>
<i>specular peak</i>	polarization decreases with increasing incident angle	polarization decreases with increasing surface roughness
<i>backscattering region</i>	polarization independent on illumination angles	polarization approaches zero with increasing surface roughness
specular peak can be used to distinguish illumination angle and surface variation for smoother surface only		

Table 7.1: The distinguishing ability of the four Mueller matrix elements for illumination angles and surface roughness .

S_{11}		
<i>position</i>	<i>non-absorbing diffuse surface</i>	<i>absorbing diffuse surface</i>
<i>backscattering region</i>	higher intensity	lower intensity
<i>other scattering region</i>	lower intensity	higher intensity
Absorbing diffuse surface has higher intensity at scattering angles except in the backscattering region		
S_{12}		
<i>position</i>	<i>non-absorbing diffuse surface</i>	<i>absorbing diffuse surface</i>
<i>backscattering region</i>	higher polarization	lower polarization
<i>other scattering region</i>	lower polarization	higher polarization
Absorbing diffuse surface has higher percent polarization at scattering angles except in the backscattering region (approaches zero)		
S_{22}		
<i>position</i>	<i>non-absorbing diffuse surface</i>	<i>absorbing diffuse surface</i>
<i>backscattering region</i>	higher polarization	lower polarization
<i>other scattering region</i>	lower polarization	higher polarization
Absorbing diffuse surface has higher percent polarization at scattering angles except in the backscattering region		
S_{33}		
<i>position</i>	<i>non-absorbing diffuse surface</i>	<i>absorbing diffuse surface</i>
<i>backscattering region</i>	lower polarization	higher polarization
<i>other scattering region</i>	higher polarization	lower polarization
Absorbing diffuse surface has lower percent polarization at scattering angles except in the backscattering region		
S_{34}		
<i>position</i>	<i>non-absorbing diffuse surface</i>	<i>absorbing diffuse surface</i>
<i>backscattering region</i>	zero polarization	nonzero polarization
<i>other scattering region</i>	zero polarization	nonzero polarization
Absorbing diffuse surface has nonzero polarization at scattering angles S_{34} is the most sensitive element for non-absorbing and absorbing diffuse surface		

Table 7.2: The distinguishing ability of the Mueller matrix elements for non-absorbing and absorbing diffuse surface.

We have found it advantageous to study light scattering from rough surfaces using systematic and controlled procedures. When a small perturbation is added to the perfect system, the matrix elements will show a particular change. When we understand the idealized system, we get insight to how a degraded system scatters. In this study, we also find that when surfaces become more complex, S_{33} and S_{34} become less sensitive to the surface variation. Therefore, these two elements are not reliable as a diagnostic tool. S_{34} is very sensitive to a change from real index of reflection (non-absorbing medium) to complex index of reflection (absorbing medium). In general, the polarization matrix elements become independent of illumination angle as the surface becomes rougher. On the other hand, the polarization matrix elements depend more on the index of refraction as the surface becomes rougher.

In reality a rough surface could be as complex as the earth's surface which is composed of many different kinds of substances (sand, soil, clay, ...). The ingredients and particle sizes can be found in Table 7.3. All have different degrees of roughness and different optical properties. The Mueller matrix elements will therefore be complicated and perhaps not reveal important information about the surface. The four Mueller matrix elements for sand, sandy soil, clay soil, and loamy soil illuminated at grazing incidence are shown from Figure 7.1 to 7.4. Which show that information loss in the four matrix elements signals creates light scattering data that are not unique to the scattering interaction. Without a doubt, the inversion will yield highly uncertain or even wrong values for this system. However, in some cases, the data are still sufficient to partially characterize the scattering system. Presently, there is no theory to predict these complex systems but the interest in

sample	clay <0.002mm	silt 0.002mm-0.05mm	sand 0.05mm-2mm
sand	2.0 %	1.7 %	96.3 %
sandy soil	12.3 %	29.0 %	58.7 %
clay soil	33.0 %	18.0 %	49.0 %
loamy soil	20.7 %	39.7 %	39.6 %

Table 7.3: Ingredient and size range of particles in four soils.

their scattering properties is very great and this is also a very important topic in remote sensing from satellites. Therefore more experimental research and theoretical study are needed before we fully understand the light scattering from such rough surfaces.

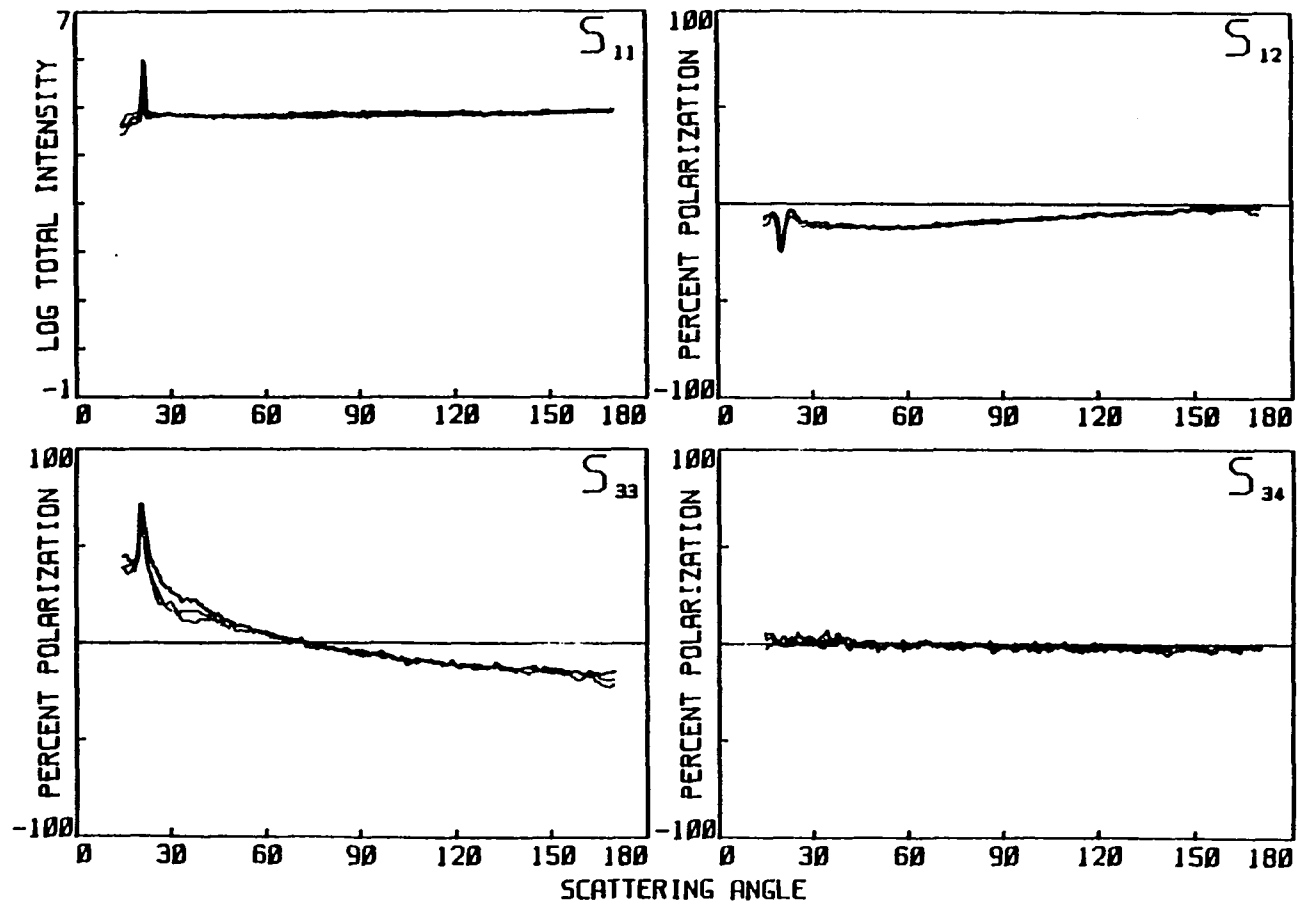


Figure 7.1: The experimentally measured Mueller matrix elements for sand measured at three different positions on the surface (illuminated at grazing incidence).

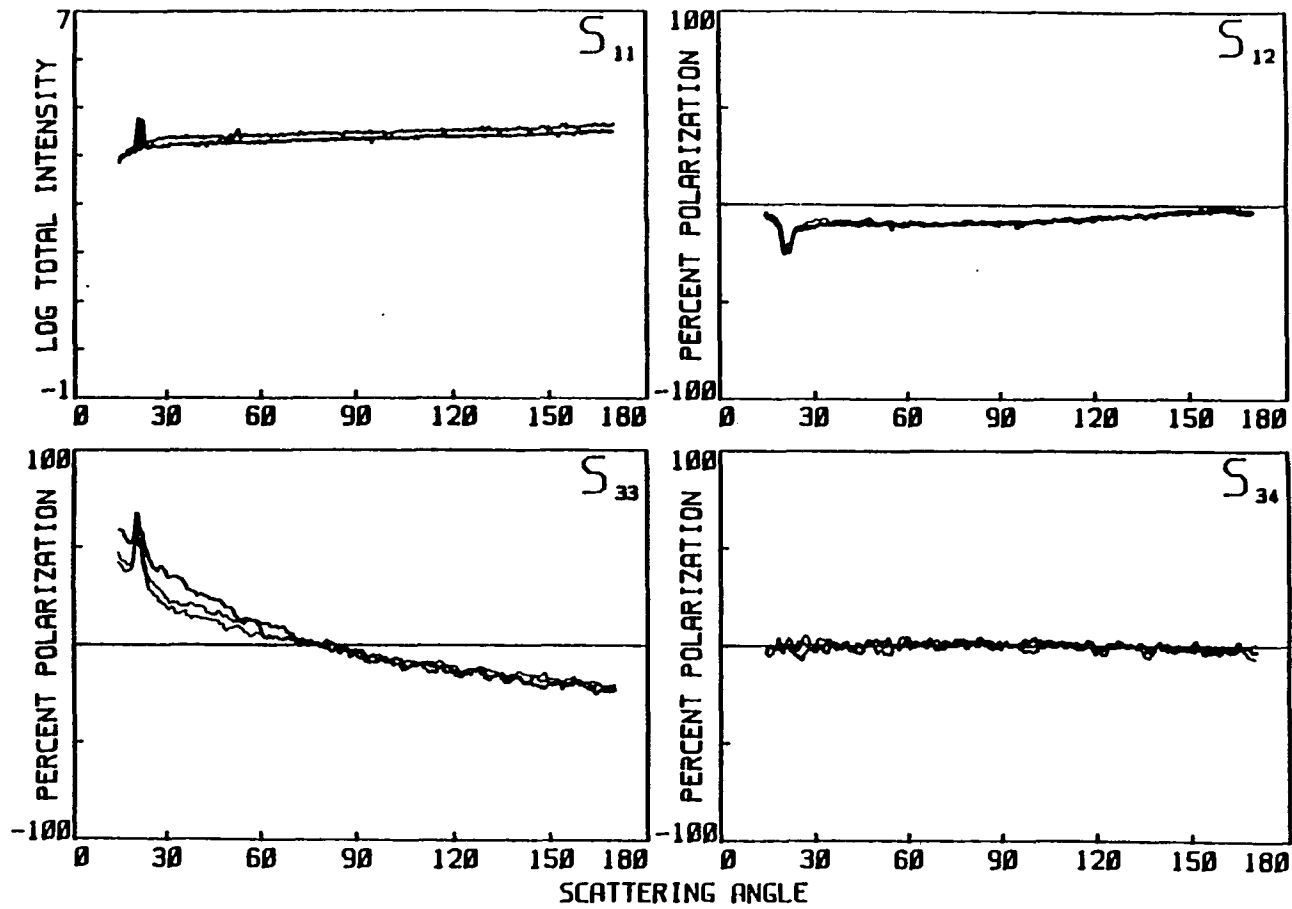


Figure 7.2: The experimentally measured Mueller matrix elements for sandy soil measured at three different positions on the surface (illuminated at grazing incidence).

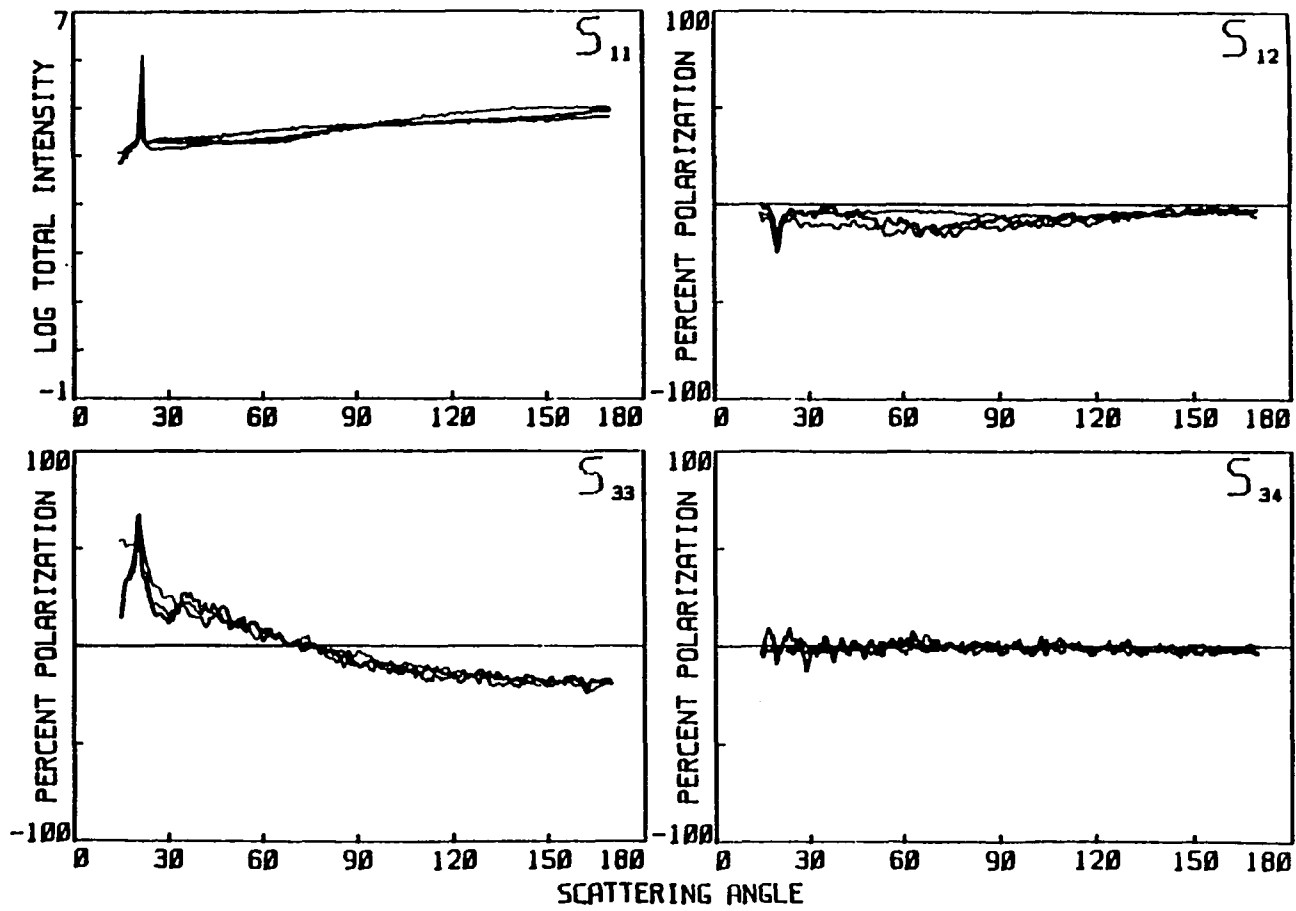


Figure 7.3: The experimentally measured Mueller matrix elements for clay soil measured at three different positions on the surface (illuminated at grazing incidence).

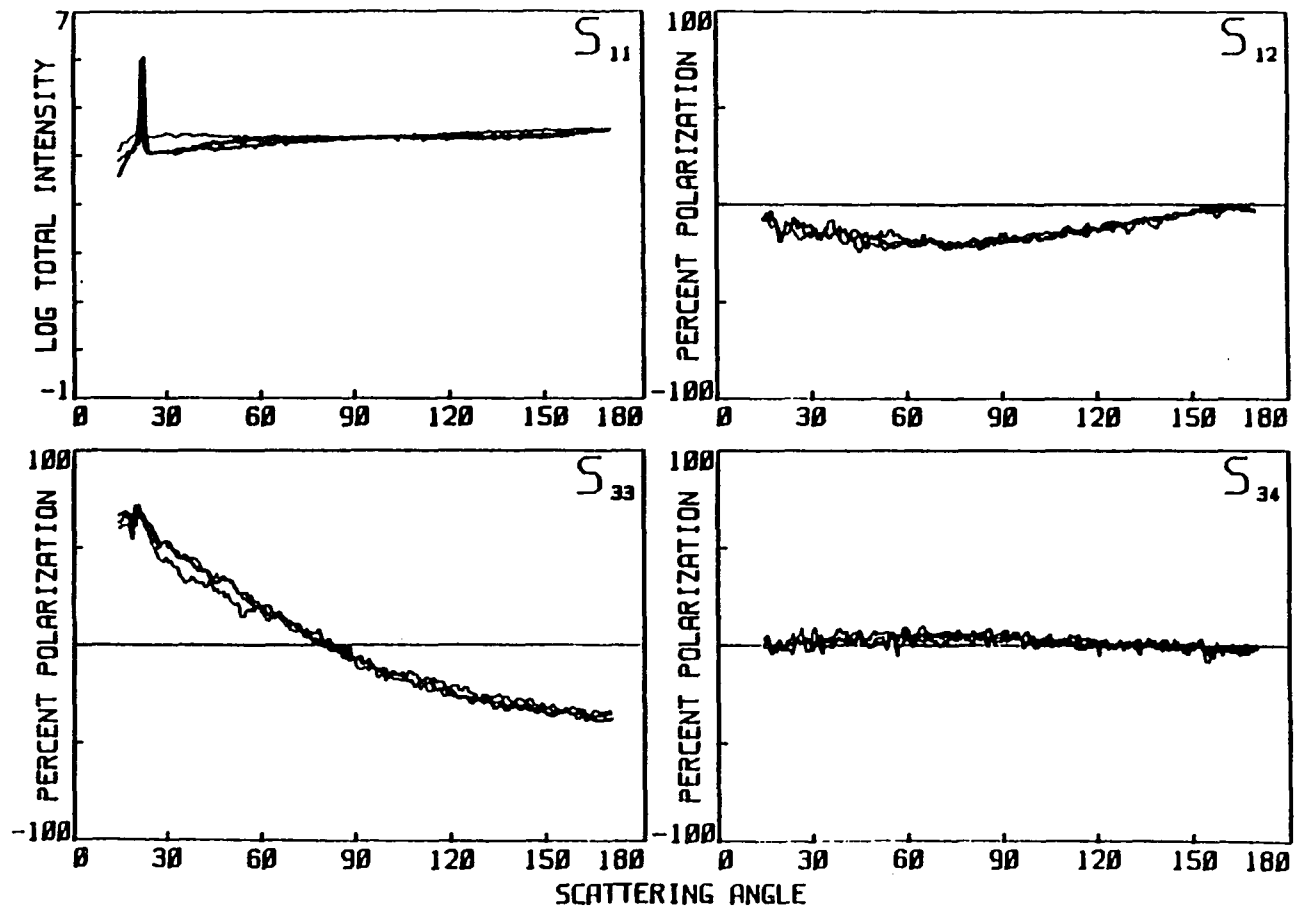


Figure 7.4: The experimentally measured Mueller matrix elements for loamy soil measured at three different positions on the surface (illuminated at grazing incidence).

APPENDIX A

SCANNING ELECTRON MICROSCOPE TECHNIQUE

A.1 Introduction

The scanning electron microscope (SEM) is one presently of the most versatile instruments available for the examination and analysis of the microstructural characteristics of solid objects. The most important reason for using SEM is due to the high resolution which can be obtained when bulk objects are examined. Values of order 50\AA are usually quoted for commercial instruments. Another important feature of the SEM is the three-dimension appearance of the specimen image, which is a direct result of the large depth of field. The greater depth of field of SEM provides much more information about a specimen. Another advantage of SEM is the wide variety of electron-specimen interactions that can be used to form an image and to furnish qualitative and quantitative information. The large depth of field, the excellent contrast, and the straight-forward preparation of solid specimens are reasons people use the SEM for the imaging of surfaces.

A.2 Principle of the Scanning Electron Microscope

The scanning electron microscope (SEM) and the electron probe microanalyzer (EPMA) are in reality very similar instruments. Therefore, several manufacturers have

constructed instruments capable of being operated as an electron microprobe and as a high resolution scanning electron microscope. Figure A.1 [15] shows a schematic of the electron and x-ray optics of such a combination instrument.

The principle of the SEM is shown in the Figure A.1. This machine consists of the electron gun and two or more electron lenses. The electron gun provides a stable source of electrons which is used to form the electron beam. These electrons are usually obtained from a source by a process called thermionic emission. Electrons from a thermionic or field-emission cathode are accelerated by a voltage of 1 to 50 KV applied between the cathode and anode. The smallest beam cross section at the gun, the crossover, with a diameter about the order of 10 to 50 μm for thermionic and 10 to 100 nm for field emission guns, is demagnified by a two or three stage electron lens system. Therefore the electron probe of diameter 1 to 10 nm carrying an electron probe current of 10^{-10} to 10^{-12} A is formed at the specimen surface. This current can be obtained from the emission current density J_c which is described by Richardson law[15],

$$J_c = A_c T^2 \exp(-E_w/\kappa T) \text{ A/cm}^2$$

where $A_c \text{ A/cm}^2 K^2$ is a constant which is the function of the material, $T(K)$ is the emission temperature, E_w is the work function of the cathode, and κ is the Boltzmann constant. For modes of operation that need a higher electron probe current of 10^{-9} to 10^{-8} A, the electron probe diameter increases to 0.1 to 1 μm .

The final object (probe forming) lens has to operate with a relatively long working distance, that is, the distance between specimen and lower pole piece, so that the various particles and quanta emitted can be collected with the desired efficiency and if necessary,

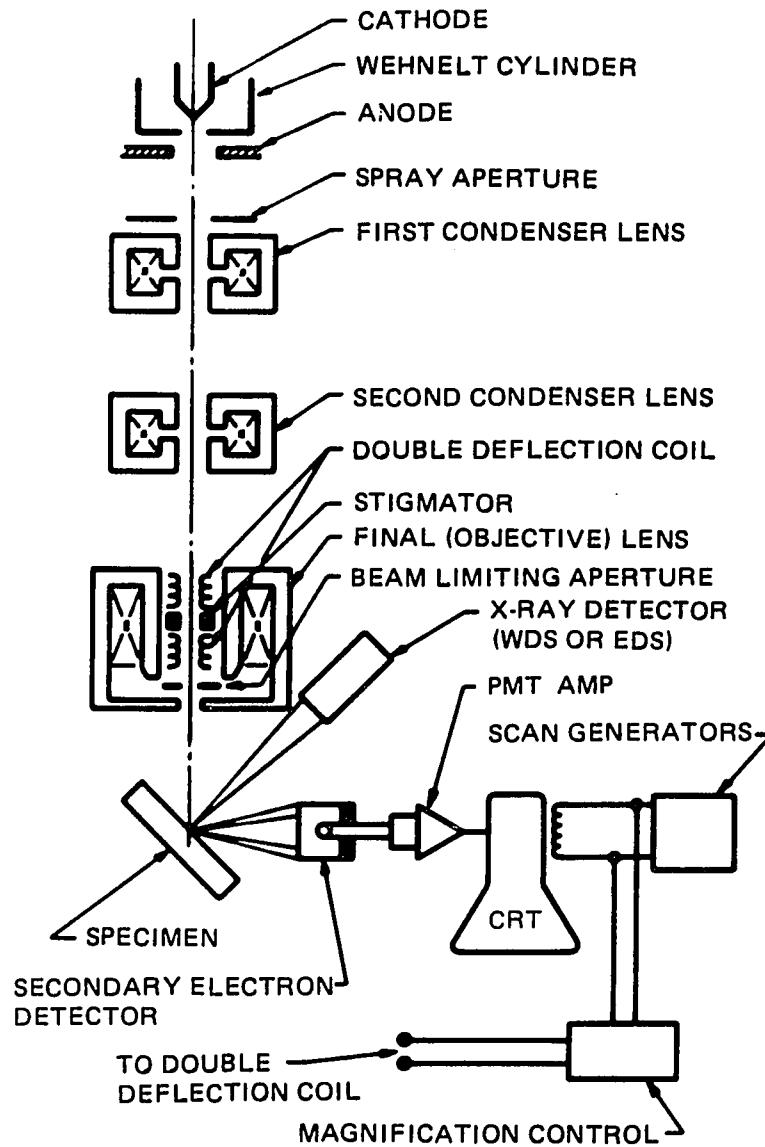


Figure A.1: Schematic drawing of the electron and x-ray optics of a combined SEM-EPMA.

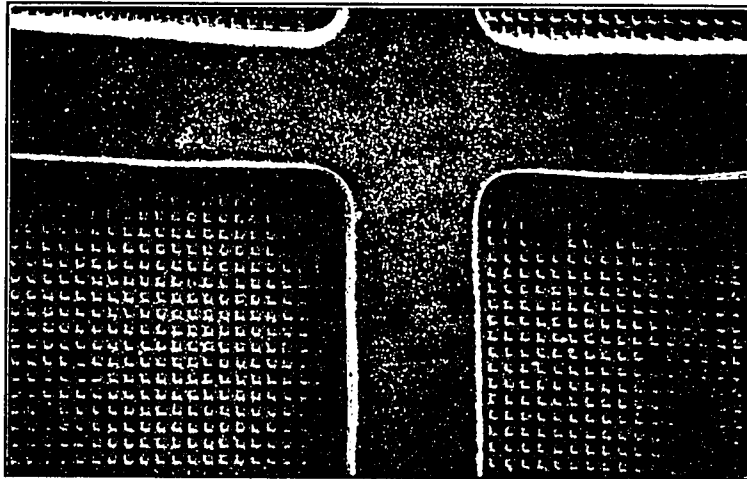
with zero magnetic field at specimen. This requirement increases the spherical aberration of the probe forming lens and, therefore, the smallest attainable electron-probe size. Electron-probe current, aperture, and size can all be varied but not independently by changing the magnetic field strength of the first condenser lenses. Apertures of the order of the milliradians are used for routine work and high resolution. One to two orders of magnitude smaller apertures are necessary to increase the depth of the field and improve the angular resolution in electron channeling patterns.

A deflection coil system in front of the last lens scans the electron probe in a raster across the specimen and in synchronism with the electron beam of a separate cathode-ray tube (CRT). The magnification can be increased simply by decreasing the scan-coil current and keep the image size on CRT constant. Figure A.2 shows the image of same specimen with two different magnification.

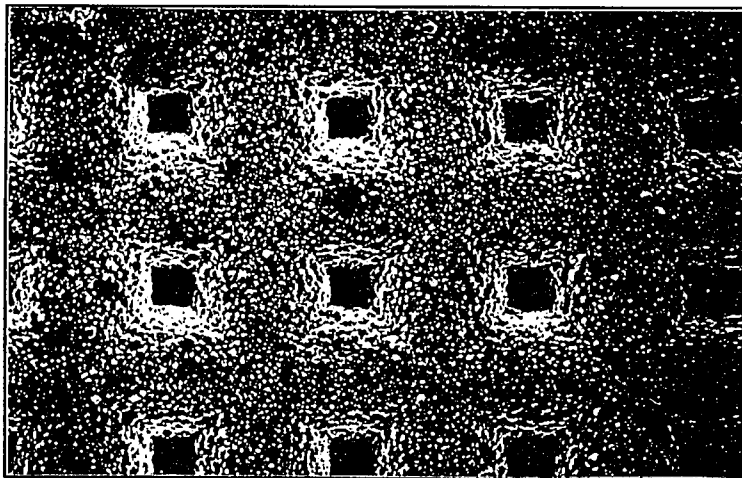
The electron-probe aperture, that is, the semi-apex angle of convergent cone of electron trajectories, is small around the order of few tens of milliradians with the result that the depth of field is much larger than in light microscopy. Therefore, specimens with large variations in depth can be sharply imaged even at lowest magnification of 20 to 50 times.

A.3 Operation Parameters of using ISI Super III-A SEM

The micrographs for each sample taken by using ISI Super III-A SEM, were shown from Figure 5.2 to Figure 5.11. The operation parameters used to take these micrographs



Magnification: 50X



Magnification: 500X



Figure A.2: Example of two different magnifications of a metal grid with symmetric geometry.

are as follows.

Instrument	: ISI Super III-A SEM
Magnification	: 100X
Bar scale	: $100\mu m$
Voltage	: middle
tilt	: 0 degree
Dynamic focus	: 0 degree
Working distance	: $8mm$
Spot size	: 1:00
Contrast	: $15\mu A$
Brightness	: $35\mu A$
Film type	: Polaroid 52
Aperture of camera	: 16

The working distance can be varied from 5 to 30 mm . As the working distance increases, magnification increases, giving a large spot size and a better depth of field. On the contrary, decreasing working distance decreases spot size and results in better resolution. The magnification on SEM is given by $M = L/l$, where L is the constant length of CRT and l is the length of the electron beam scan on sample. This magnification can be read from the display.

REFERENCES

- [1] Iafelice, Vincent J. and Bickel, William S., "Polarized Light-scattering Matrix Elements for Select Perfect and Perturbed Optical Surfaces," *Appl. Opt.* **26**,2410 (1987).
- [2] Hecht, Eugene, *Optics*, 2nd ed. (Addison-Wesley, Reading Massachusetts 1987).
- [3] Jackson, John David, *Classical Electrodynamics*, 2nd ed. (Wiley, New York, 1975).
- [4] van de Hulst, H.C., *Light Scattering by Small Particles* (Wiley, New York, 1957).
- [5] Bohren, Craig F. and Huffman, Donald R., *Absorption and Scattering of Light by Small Particles* (Wiley, New York, 1983).
- [6] Hunt, A. J. and Huffman, D. R., "A New Polarization- Modulated Light Scattering Instrument," *Rev. Sci. Instrum.* **44**, 1753 (1973).
- [7] Bickel, W. S., Davidson, J. F., Huffman, D. R., and Kilkson, R. "Application of Polarization Effects in Light Scattering: A New Biophysical Tool," *Proc. Natl. Acad. Sci. USA* **73**, 486 (1976).
- [8] Bell, B. W., "Single Fiber Light Scattering Matrix: An Experimental Determination," M.S. Thesis, Department of Optical Sciences, U. Arizona (1981).
- [9] Iafelice, V. J., "The Polarized Light Scattering Matrix Elements for Select Perfect and Perturbed Surfaces," M.S. Thesis, Department of Physics, U. Arizona (1985).
- [10] Kemp, James C., "Piezo-Optical Birefringence Modulators: New use for a Long-Known Effect," *J. Opt. Soc. Am.* **59**, 950 (1969).
- [11] Born, Max and Wolf, Emil, *Principles of Optics* (Pergamon Press, New York, 1980).
- [12] Heavens, O. S. *Optical Properties of Thin Solid Films* (Dover, New York, 1965).
- [13] Kortüm, Gustav, *Reflectance Spectroscopy* (Springer-Verlag, New York, 1969).

- [14] Bickel, William S., Yousief, Hashim A., and Bailey, Wilbur M., "Masking of Information in Light Scattering Signals from Complex Scatterers," *Aerosol Science and Technology* **1**, 329-335 (1982).
- [15] Goldstein, J. I., Newbury, D. E., Echline, P., Joy, D. C., Fiori, C., Lifshin, E., *Scanning Electron Microscopy and X-Ray Microanalysis* (Plenum Press, New York, 1981).